Journal of Thermal Analysis and Calorimetry (2023) 148:3089–3115
https://doi.org/10.1007/s10973-022-11637-5

Secondary flow structure characteristics of an automotive mixed flow turbocharger turbine volute at different aspect ratios

A. Azmi[1,2] · M. H. Padzillah[1]

Received: 30 January 2022 / Accepted: 17 September 2022 / Published online: 11 November 2022

Abstract

This paper presents an experimentally validated numerical analysis of the influence of volute aspect ratio (VAR) on the fluid flow characteristics of a volute in a mixed flow turbine. The geometry of the volute subjects the flow to centrifugal forces that affect the vertical motion of the fluid, commonly known as secondary flow, which is fundamentally opposed in straight channels commonly associated with the primary flow. The flow characteristics were analysed for four-volute designs with constant volute area-to-centroid radius ratio (A/r) but with different VARs ranging from 0.5 to 2.0 at selected circumferential positions under steady state at different operating conditions. Secondary flow structure characteristics were identified based on pressure contours, velocity contours and streamlines. The internal volute flow structure was found to be dependent on the VAR. The results show corner and counter-rotating Dean effect-type vortices at higher volute aspect ratios. In addition, the results also show that as the pressure ratio increases, the deflection of primary flow increases and at certain positions, flow separation occurred. The resulting secondary flow structures that exist in the volute are strongly influenced by the VAR at different operating conditions, thus affecting turbine performance.

Keywords Mixed flow turbocharger · Secondary flows · Computational fluid dynamic · Variable geometry · Turbine volute

List of symbols

Roman symbols

A/r	Ratio of volute cross section area and the radial of its centre (mm)
b/h	Ratio volute cross section width and height
CFD	Computational fluid dynamics
MFP	Mass flow rate parameter (kg s^{-1} $\sqrt{K}$)/Pa
PR	Pressure ratio
VR	Velocity ratio
VAR	Volute aspect ratio
RMS	Root mean squared
rpm	Rotations per minute
C	Turbine absolute velocity (m s^{-1})
C_m	Meridional velocity (m s^{-1})
C_θ	Flow velocity
$\dot{m}$	Mass flow rate (kg s^{-1})
r_n	Radius of volute cross section to rotational axis (m)
R	Radius of volute discharge to rotational axis (m)
N	Rotational speed (rpm)
T	Temperature (K)
p	Pressure (Pa)
t	Time (s)
U	Flow velocity
$\dot{W}$	Power (W)
y^+	Non-dimensionalized distance from wall

Greek symbols

α	Absolute flow angle
η	Efficiency
∇	Vector differential operator
v	Kinematic viscosity (m s^{-1})
ρ	Density (kg m^{-3})
θ	Angle (°)
π	Pi parameter
τ	Torque (Nm)

✉ M. H. Padzillah
mhasbullah@utm.my

[1] UTM Centre for Low Carbon Transport in Cooperation With Imperial College London, Universiti Teknologi Malaysia, 81300 Skudai, Johor Bharu, Malaysia

[2] Plant Engineering Technology (PETech) Section, Universiti Kuala Lumpur - Malaysian Institute of Industrial Technology (UniKL MITEC), Persiaran Sinaran Ilmu, Bandar Sri Alam, 81750 Johor, Malaysia

Subscripts

1	Volute inlet
2	Volute exit/nozzle inlet
in	Inlet
out	Outlet
act	Actual
isen	Isentropic
m	Meridional directional component
t	Turbine

Introduction

Global warming is a result of the annual emission of some 50 billion tonnes of greenhouse gases (GHG) [1]. A significant portion of this is due to human activity with the largest single source being the emissions from the burning of fossil fuels in internal combustion engines (ICEs) from all forms of transport [2]. The current trend towards conventional fuel driving shows that ICEs are still important until alternative energy vehicles become the norm [3, 4].

To reduce the impact of emissions from ICEs, it is necessary to meet the challenges of stringent regulations for exhaust gas emissions and improvement of its overall fuel efficiency. The turbocharger is an effective technology for improving fuel consumption in internal combustion engines by reducing the waste heat losses from the exhaust gasses [5–11]. The turbocharger consists of a turbine that is powered by the engine exhaust to power the compressor to increase air pressure and thus allow more air into the cylinders for more efficient combustion. The turbine, an important component of a turbocharger, comprises of three main components, namely a volute, a rotor and a nozzle. While the rotor design is critical to the shaft power [12], a better understanding of flow behaviour in the turbine volute passage is required to improve energy extraction from the exhaust gas and minimize entry losses into the rotor resulting in improved efficiency of the turbocharger and therefore the ICE itself.

In trying to improve the total performance of the turbocharger turbine, the turbine volute has been the subject of several research projects. As the volute is the bulkiest component of the turbine, manufacturers require more compact designs for the volute to minimize costs, and a suitable compromise between performance and costs must be found. It is therefore necessary to study the effect of the cross-sectional shape of the turbine volute in order to determine the optimal shape that balances costs and performance.

The flow in the volute is complex with the exhaust gas undergoing rotation and then acceleration around the edge of the volute before recirculation flow occurs under the tongue as it flows into the rotor wheel generating the shaft power for the compressor. According to [13, 14], volute configuration has a strong impact on the overall performance of a turbine because its stability, operating range and location of the best efficiency point are influenced by the volute design. Experiments made by Barnard and Benson [15] on two different volute profiles showed up to 1.5% variation in turbine efficiency.

In an ideal dimensional design procedure of a volute, based on the conservation of angular momentum, or free vortex, and mass for adiabatic compressible flows, the area–radius ratio (A/r) is the most important parameter. The area–radius ratio determines the change in the flow angle at the volute exit region, thereby defining the incident angle to the rotor inlet which defines the best efficiency point. Therefore, most of the volute design effort is in the determination of the optimal distribution (A/r) in the circumferential direction. Japikse and Baines [16] indicated that for a fluid in equilibrium, to achieve a uniform mass flow distribution around the volute, the linear relationship between the cross-sectional area and the mean radius through the azimuth angle must be met. As stated in [17], the authors suggest that the volute design must be a linear reduction of the cross-sectional area and centroid radius. Bhinder [18] asserted that a non-uniform flow distribution at the rotor inlet caused by changes in flow angle can be avoided if the a linear reduction area–radius ratio (A/r) is a linear function of the azimuth angle. However, the equations and the assumptions used by Bhinder [18] are given a different interpretation from the results he obtained on the graphs of radial area ratio (A/r) versus azimuth angle for three different volute configurations. In each of the curves, it turns out that there is a large variation in the flow angle.

In general, the inlet of a turbine rotor is a feed with a rotational flow accelerated by a volute at the desired angle to optimize turbine performance. Defining the desired operating inlet conditions is the initial phase of the turbine design procedure. Accordingly, optimization of the volute design procedure was then carried out, followed by a three-dimensional computational fluid dynamics analysis of the design. This is necessary as the flow in the volute is three dimensional and turbulent. However, despite being able to create good theoretical volute performance, there is usually a need to consider installation requirements [19–21].

Due to the importance of volutes, since the 1990s there has been much research on volutes and especially on turbine volute design procedures. In addition, over time these studies were not limited to theory and experiment [17, 18, 21–24] but by the priority for highly efficient engines. More studies on turbine volutes are performed using the CFD numerical approach [19, 20, 25–33] to correctly predict the flow behaviour in turbine volutes over a wide range of operating conditions.

Theoretical and experimental volute flow field analysis was carried out by [17] and [24]. In cases where a

three-dimensional flow field exists, the flow is often viewed as having two components, a primary flow and a secondary flow. The primary flow is parallel to the main direction of fluid movement, and the secondary flow is perpendicular to it. The geometry of the volute subjects the flow to centrifugal forces that affect the vertical motion of the fluid, commonly known as secondary flow. The investigation by [21] considered the development of a flow structure in a series of volute passages from the inlet, the volute passage to the volute discharge. There is a clear occurrence of the flow deflection of the primary flow which then gives rise to the creation of a secondary flow around the volute passage. The velocity and trend component profiles were plotted to show the flow characteristics at each volute passage radial ratio across the azimuth angle. In an investigation of the interaction between the volute and the rotor during measurement carried out [24], the authors concluded that the appearance of a secondary flow in the volute passage can cause a loss of energy that is directly related to the stage performance. They also concluded that non-uniform mass flow distribution around the rotor contributes to poor performance.

In addition, to the experimental approach, a number of studies, Refs. [19, 29–33], have used the same numerical CFD method in volute flow field analysis but with different findings. Martinez-Botas et al. [29] used a k-epsilon turbulence model of two equations and have observed on the volute plane between azimuth angles of 45° and 270°, the strong appearance of the secondary flow structure disappears towards the centre of the circular cross-sectional volute. Consistent with Yang et al. [19], the presence of secondary flow structures has always been associated with energy loss. Moreover, high pressure loss is recorded when the flow moves towards the sharp corner of the discharged volute. Simpson et al. [30] have also performed both steady and unsteady state full-stage CFD simulations on different radial turbine configurations. The authors successfully captured the secondary flow structure in the volute outlet and found no vortex formed in the first half of the volute until at about 90°, and thereafter, the presence of a counter-rotation vortex was observed formed in the upper region of the trapezoidal shaped cross section of the volute passage, causing an increase in losses detected along the end wall.

The effect of volute cross-sectional shape was also studied by [19] using two asymmetric volutes of different aspect ratios (width, b and height, h). The results show that changes in the volute design resulted in significant variations in the volute secondary flow structure and stage performance. They also showed that a complex secondary flow structure in both volute configurations, consisting of vortices of varying sizes, contributed to the entropy generation discrepancy in the volute. However, no explanation for their formation is given. Furthermore, comparisons were made only on one aspect ratio of optimized volute A against the baseline volute B. Different volute aspect ratios need to be analysed and compared in order to find the optimal aspect ratio (b/h). In addition, a systematic comparative approach should be used by analysing various constant aspect ratios across the circumference azimuth angles. From the experimental results, Ref. [19] concluded that turbines with optimized volute A have better average cycle efficiency under pulsed conditions for different loads and frequencies. However, this needs to be analysed further because the optimum aspect ratio (b/h) is the most independent parameter in achieving the best efficiency.

The study by Lee et al.[31] used more numerical analysis to study the structure of volute secondary flow under both steady-state and pulsed flow conditions. In this case, the authors studied the secondary flow in volutes by comparing three symmetric designs of circular shape volute aspect ratios of 0.5, 1, and 2. Secondary flows in volutes are studied and explained in terms of Dean's effects and their development through the volutes investigated. The effect of volute design on rotor input variation is investigated in detail to understand the effect of volute design on rotor performance. The results show that the secondary flow structure shows an attractive interaction of the central and wall bound flow. In parallel, they also found that the volute aspect ratio can have a significant effect on the mass flow parameter (MFP) when the ratio of volute cross-sectional area to the volute centroid radius (A/r) is kept constant. However, the effect of the three circular cross sections on the turbine efficiency was low, and no further information was given on achieving the optimum turbine efficiency. They also observed a vortex was found to exist at about 54° late in the first half of the volute but disappeared around the volute passage theoretically similar to the Dean-like effect. However, it was found that this study lacked experimental validation and further extensive parametric studies are required.

Moreover, Lee et al. [33] further performed a numerical analysis to investigate the effect of four-volute designs on turbine performance. The first two (2) volute designs are with the same A/r but with different aspect ratios (AR) (width, b/height, h) each with AR = 0.5 and AR = 2. Meanwhile, two (2) more volute designs are with both volutes tilted. The study showed that the large secondary flow at AR = 0.5 reduced the turbine performance. In addition, the inclining the volute resulted in an asymmetric flow structure and the authors concluded that combining the ideas of low AR and tilting the volute result in reduced turbine performance and therefore not beneficial. Meanwhile, similar studies have been conducted by Meghnine M.A [32]. In this study, an investigation of four asymmetric volute geometry shapes was conducted to analyse the flow characteristics in the volute and to estimate its effect on the performance of mixed flow turbines. The authors found the appearance of vortices in each volute design and concluded that the

number of vortices can be reduced when the volute volume is reduced.

Volute design

The fundamental assumptions in the volute design procedure are based on the conservation application of angular momentum, or free vortex, uniform mass distribution around the volute.

Figure 1 shows a schematic diagram of turbine volute used in this research study. The conservation of angular momentum, or free vortex, equation may be expressed as:

$$r_\theta \cdot C_\theta = \text{constant} = K \tag{1}$$

where θ = azimuth angle (°) from the tongue; r_θ. = centroid radius of the section at azimuth angle; C_θ = tangential velocity at azimuth angle.

For a fluid in equilibrium, the continuity equation for the mass flow through any cross-sectional plane at azimuth angle θ is

$$\dot{m}_\theta = \rho_\theta \cdot A_\theta \cdot C_\theta \tag{2}$$

For a uniform distribution of mass flow around the volute, the ratio mass flow rate is the function of azimuth angle that can be written as:

$$\dot{m}_\theta = m\left(1 - \frac{\theta}{2\pi}\right) \tag{3}$$

By substituting Eqs. (1) and (3) in Eq. (2), the Eq. (4) can be defined as:

$$\frac{A_\theta}{\theta} = \frac{\dot{m}}{\rho_\theta} \cdot \frac{1}{K}\left(1 - \frac{\theta}{2\pi}\right) \tag{4}$$

where r_θ = centroid radius of the cross section at azimuth angle θ.

As the variations in density are relatively small, the area–radius (A/r) ratio in Eq. (4) must be a linear function of the azimuth angle as well the volute exit flow angle (α_2), resulting in the following expressions:

$$\frac{A_\theta}{r_\theta} = f(\theta) \tag{5}$$

$$\tan\alpha_2 = \frac{C_{\theta 2}}{C_{r2}} \tag{6}$$

By substituting Eqs. (1) and (2) in Eq. (6), the volute exit flow angle may be defined as a function of the area–radius (A/r) ratio and density ratio.

$$\tan\alpha_2 = \frac{\rho 2}{\rho 1} \cdot \frac{A_2/r_2}{A_1/r_1} \tag{7}$$

Hence, the important geometric parameters in volute design based on the assumptions of uniform mass distribution, and equilibrium flow A/r and $\tan\alpha_2$ are given in Eq. (4) and (7), respectively. Indeed, there are only a few studies that analyse the flow field structure in turbine volutes, and there should be more research done on this field in the future to gain a better understanding of the effect of volute flow fields on turbine performance.

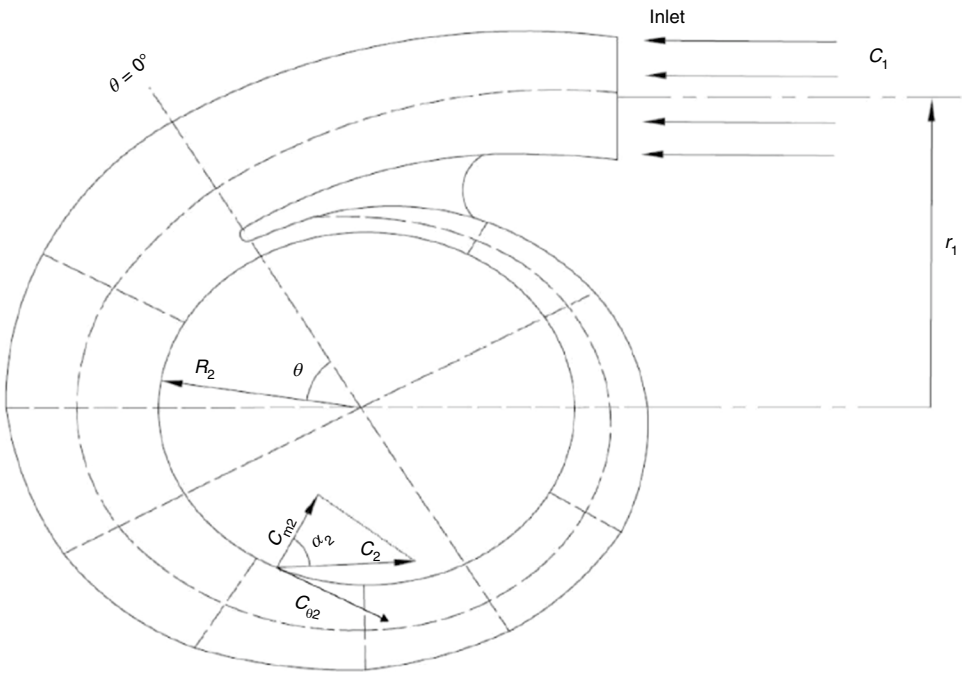

Fig. 1 Mixed flow turbine volute

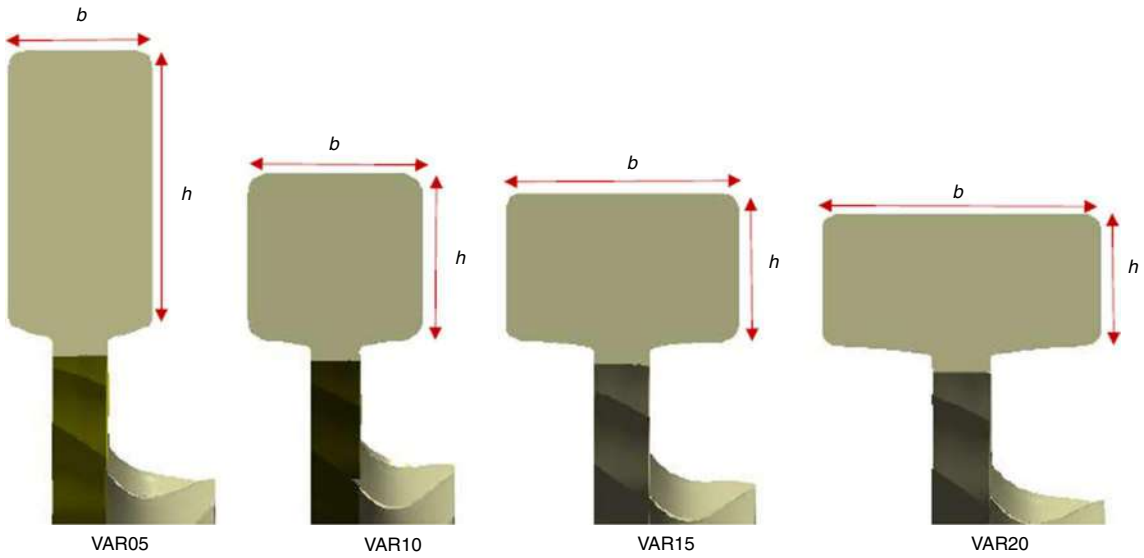

Fig. 2 The cross-sectional shape of symmetrical rectangular cross sections of each

Table 1 The parametric study for each volute aspect ratio (VAR)

Volute	Aspect ratio	Low mass flow/kg s^{-1}	Design mass flow/kg s^{-1}	High mass flow/kg s^{-1}
VAR05	0.5	–	–	–
VAR10	1		–	–
VAR15	1.5	–	–	–
VAR20	2		–	
Baseline			–	

Volute geometry

This paper aims to describe the development of secondary flow within a rectangular cross-sectional volute, with rounded end corners, under steady state at different operating conditions. In this research study, the volute geometry used is the modified Holset H3B volute designed by Rajoo [11] with the volute aspect ratio (VAR) ranging from 0.5 to 2.0. The parameters studied are shown in Fig. 2 and Table 1, which shows the operating conditions studied for each volute geometry. The area–radius ratio as a function of azimuth angle is given in Fig. 3. Information on the dimensions of the optimized Holset H3B volute is shown in Fig. 4. The four design volutes studied are named VAR05, VAR10, VAR15 and VAR20. The *A*/*r* circumferential distribution was designed to be the same for four volutes; however, their cross-sectional shape is different. The volute aspect ratio (*b*/*h*), which refers to ratio of the width over the height of the cross section, is used to describe the individual volute geometries. A systematic comparison of the performance of the four volutes is made by maintaining a constant VAR for all azimuth angles, see Fig. 5. This allows the optimum aspect ratio, width to height ratio, to be determined. No such study has been made to date with respect to the improvement of a turbocharger turbine performance, highlighting the originality of the current work.

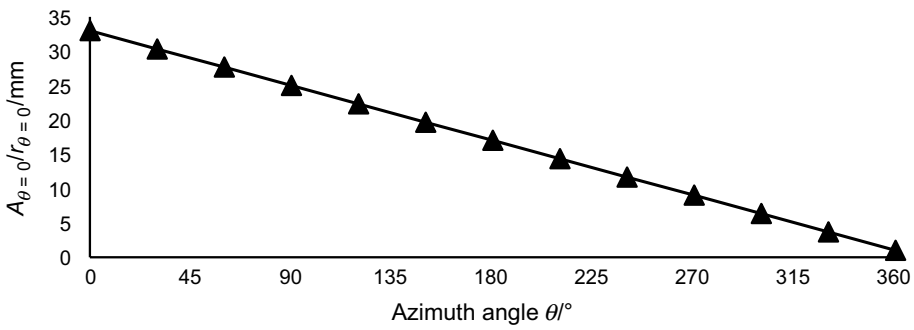

Fig. 3 Volute area-to-centroid radius ratio (*A*/*r*) as a function of azimuth angle

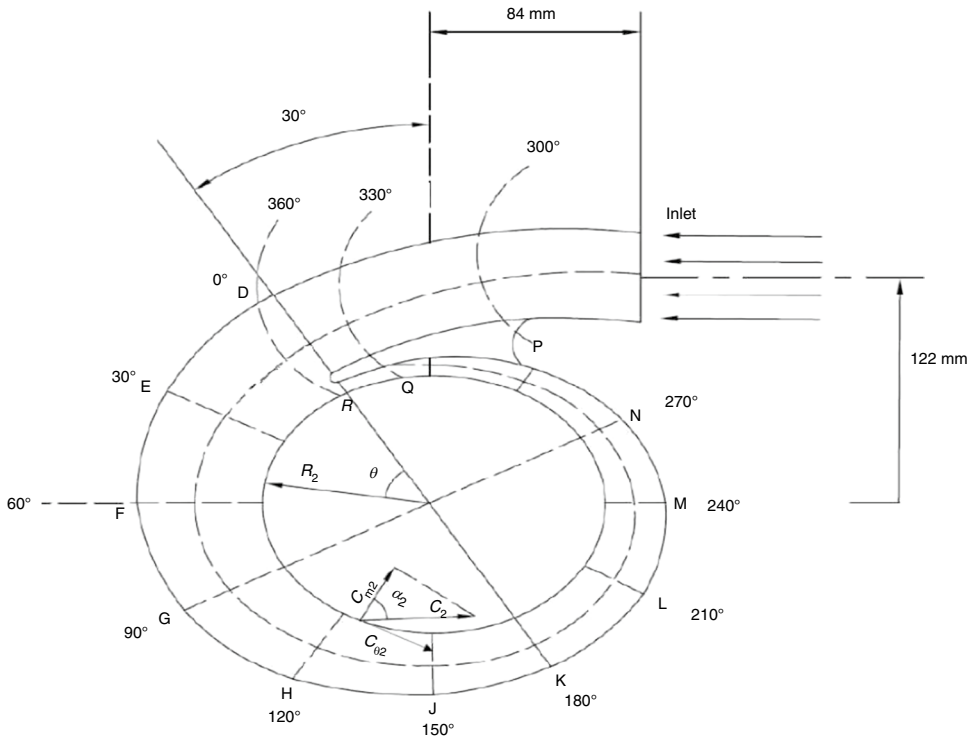

Fig. 4 The dimensions of the volute

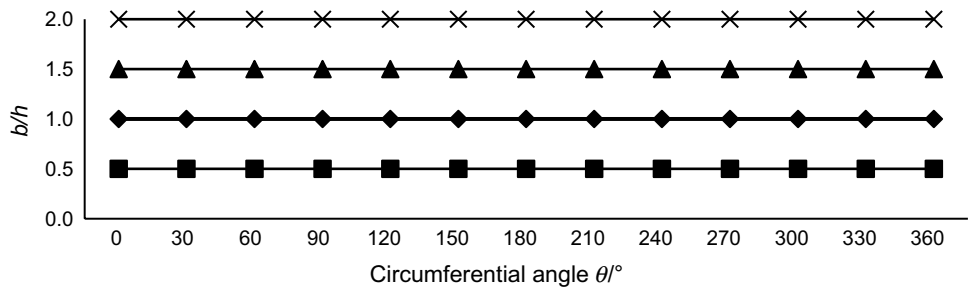

Fig. 5 Aspect ratio (b/h) of the four volutes

Research methodology

Experimental

In this study, experimental data of [34] were used for the validation of the CFD modelling. The experimental data used by [34] were obtained using the cold-flow turbocharger test facility available at Imperial College London. This facility utilizes the 'similarity approach' developed by Glassman [35] in order to get equivalent conditions to actual hot operating condition in a vehicle while using ambient air. A schematic of the cold-flow turbocharger test facility is shown in Fig. 6.

Air is supplied to the facility by a centrally housed compressor system, which consists of three Ingersoll Rand screw type compressors, capable of delivering up to 1 kg s^{-1} compressed air at maximum pressure of 5 bars (absolute) to an air receiver. Air from the receiver is filtered through a three-stage cyclone and is then fed under flow control to the turbine. A safety valve provides protection in the event of any high pressure. The air is then heated to ensure that no water condensation occurs during expansion in the turbine.

Downstream of the heater the flow is split into two separate pipes each with its own flow controller to allow for unequal flow through each pipe. The flow in each pipe is measured using an orifice type meter. The flows in each limb are then directed to a rotating chopper-plate type t pulse generator used to facilitate unsteady state testing. During steady operation, the chopper plates are left in the fully open position. Downstream of the pulse generator is the measurement plane where averaged and instantaneous flow, temperature and pressure are measured so that it is possible to calculate the isentropic energy available to the turbine. The connecting duct then connects the measurement plane and the volute

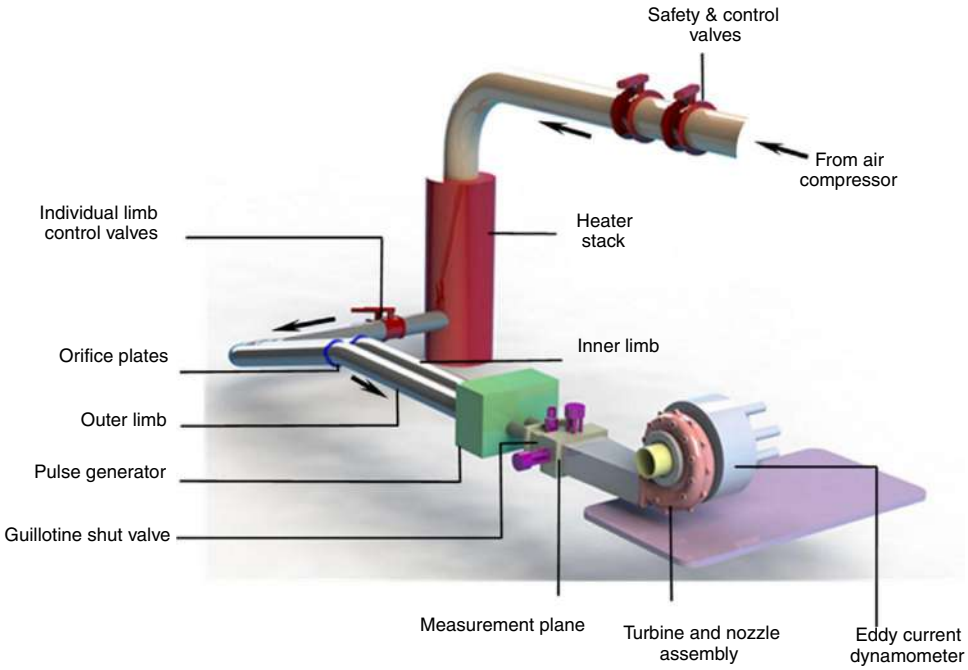

Fig. 6 Schematic of turbocharger test facility at Imperial College London [34]

inlet. This duct may be either a converging duct to merge the flows from the two limbs into a single-entry volute, as used in this research, or it could also keep the flows separated for a multiple entry volute.

The turbine is directly connected to a high-speed eddy current dynamometer capable of speeds up to 60 k rpm and dissipating more than 60 kW of shaft power. The eddy current dynamometer is water cooled. The dynamometer is instrumented with a load cell and optical speed sensor for the direct torque and speed measurement, respectively.

Numerical modelling

In this study, the turbine volute was analysed numerically to investigate the flow field details of the four-volute configurations. A complete three-dimensional CFD model is developed for each volute based on a modified Holset H3B nozzled mixed flow turbine unit. The computational results are used to compare the fluid flows within each of the volute designs. A commercial Computational Fluid Dynamics (CFD) package, Ansys CFX, was utilized for the current study. The addition of the Reynolds stress terms to Reynold's equation results in a

closure problem which is solved using a $k-$epsilon $(k-\varepsilon)$ turbulent model. By using the $(k-\varepsilon)$ turbulent model, the turbulent boundary layer near the wall region is kept at wall proximity $(y+<50)$. Fluid flow is governed by a few analytically derived equations based on conservation of mass, momentum, and energy. In general, CFD solves the discretized form of the partial differential equations, principally the continuity equation and the momentum or Navier–Stokes equations.

For a unit volume, the continuity equation can be expressed as:

$$\frac{\partial \rho}{\partial t} + \nabla \cdot (\rho U) = 0 \tag{8}$$

Assuming incompressible flow, this equation can be simplified to

$$\nabla \cdot U = 0 \tag{9}$$

Meanwhile, the momentum or Navier–Stokes equations can be written as:

$$\frac{DU}{Dt} = -\frac{1}{\rho}\nabla p + \nu \nabla^2 U \tag{10}$$

The inlet pipe and volute models are meshed using an unstructured hexahedral mesh developed in ICEM CFD package as seen in Fig. 7a, while the rotor and vane are meshed using a structured hexahedral mesh in ANSYS Turbo Grid. All the discretized geometries are assembled, and the interfaces between the geometries are specified as shown in Fig. 7b. In the steady analysis, the frozen rotor approach is used for the interface between nozzle (stationary domain) and rotor wheel (rotating domain) to account for the turbine rotation. The final assembly of a full turbocharger turbine stage and distributions of the nodes within each domain and are shown in Fig. 7 and Table 2, respectively. Before final assembly of the full model for the turbocharger, a mesh study was carried out on the baseline CFD geometry to check convergence level and determine

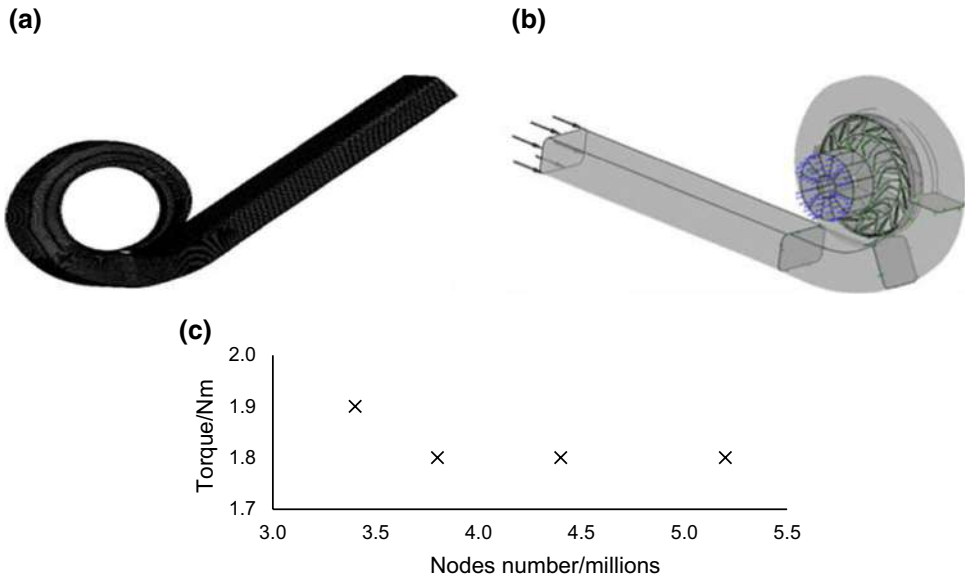

Fig. 7 **a** Final meshing and assembly of the volute section; **b** assembly of the domains in Ansys CFX-Pre; **c** meshing results

Table 2 Distribution of the computational nodes in the domain in CFD baseline volute

Geometry	CFD baseline	Type of mesh
Inlet pipe	919,600	Unstructured Hexahedral
Volute	1,028,293	Unstructured Hexahedral
Vane	995,460	Structured Hexahedral
Rotor	2,257,944	Structured Hexahedral
Total	5,201,297	

the distribution of nodes in each domain. The mesh convergence is set up to stop when the value of RMS residuals fell below 1×10^{-4}. The final mesh study results for the baseline case for the volute, rotor and vane domain are presented in Fig. 7c. For the grid independence test, the flow parameter of torque was selected to show the mesh convergence level. As indicated in Fig. 7c, for mesh sizes greater than 3.5 million cells, the torque convergence level is stable with a constant convergence trend of 1.8 Nm. As a result, approximately 5.2 million mesh nodes are used to model the turbocharger turbine domain including the inlet pipe, volute, vane, and rotor.

To assess the accuracy of the CFD method, validation of the CFD volute aspect ratio (VAR) model is performed against the CFD baseline and experimental data. Currently, this paper focuses on the validation for steady conditions using the following parameters: the turbine pressure ratio, velocity ratio, mass flow parameter, and efficiency.

Results and discussion

Model validation

The CFD model has been validated, against the experimental data of [34] by comparing the calculated turbine performance parameters, namely the turbine mass flow parameter (MFP), pressure ratio (PR), efficiency (η_t), and velocity ratio(VR) with available experimental data. The inlet total pressure and inlet total temperature are imposed as inlet boundary conditions, while the area-averaged static pressure was used as the turbine outlet boundary condition. The calculations are made for the turbine rotating at 50% of design speed (30,000 rpm). A comparison of the calculated and experimental data for turbine efficiency and mass flow is shown in Fig. 8. From the figure, it can be seen that the calculated performance of both efficiency and mass flow agrees well with the experimental data within the tested range. The CFD calculated mass flow is slightly lower than the experimental data at pressure ratios (PR) between 1.3 and 1.7 (see Fig. 8a). The calculated turbine mass flow parameters (MFP) and the pressure ratio (PR) are determined using Eqs. (11) and (12):

$$\mathrm{MFP} = \frac{\dot{m}\sqrt{T\ \mathrm{inlet}}}{P\ \mathrm{inlet}} \tag{11}$$

$$\mathrm{PR} = \frac{\dot{W}_{\mathrm{act}}}{\dot{W}_{\mathrm{isen}}} \tag{12}$$

Figure 8b shows the CFD calculations predict a slightly higher efficiency value, when compared to

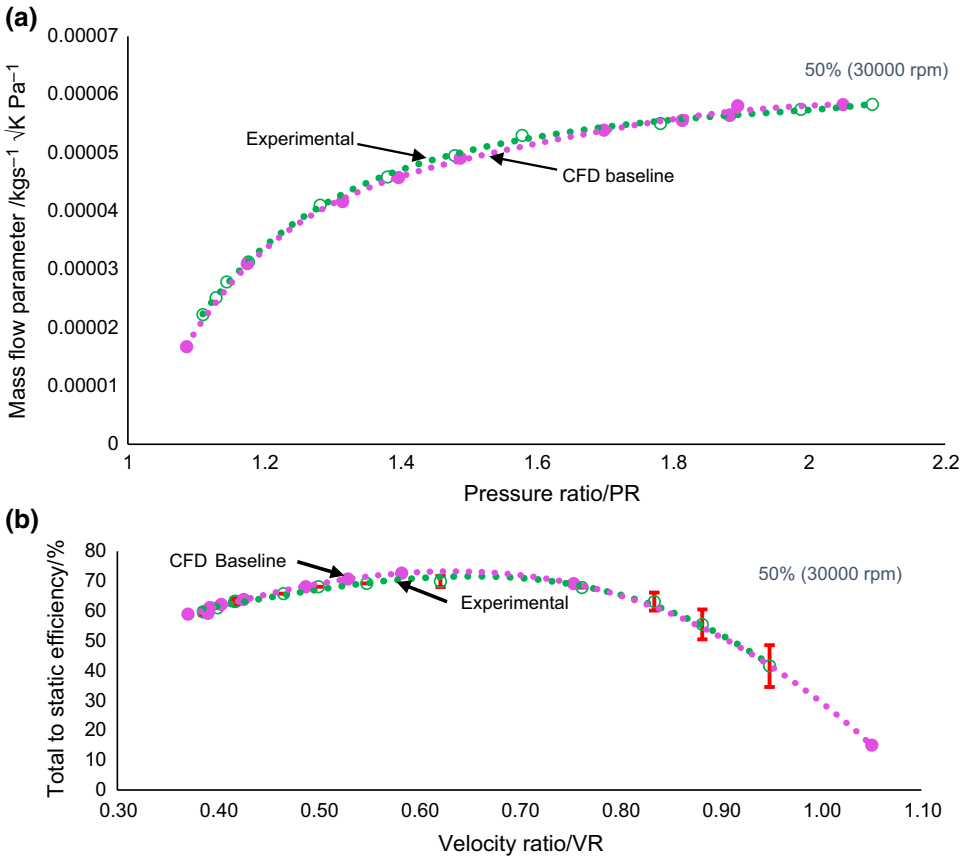

Fig. 8 Comparison between the steady turbine performance map of **a** mass flow parameter against pressure ratio and **b** total-to-static efficiency against velocity ratio between experiment and CFD calculations

the experimental data, for velocity ratios in the range 0.49–0.75. The efficiency and the velocity ratio (VR) are calculated as follows:

$$\eta_t = \frac{\dot{W}_{act}}{\dot{W}_{isen}} \tag{13}$$

where,

$$\dot{W}_{act} = 2\pi N\tau \tag{14}$$

$$\dot{W}_{isen} = \dot{m}c_p T_{in}\left(1 - \left(\frac{p_{out}}{p_{in}}\right)^{\frac{\gamma}{\gamma-1}}\right) \tag{15}$$

$$\mathrm{VR} = \frac{U}{C_{isen}} \tag{16}$$

The differences between the calculated and experimental results may be due to the assumption that parameters such as specific heat C_p and specific heat ratio γ are assumed constant. It was believed that the discrepancies from the experimental data occurred because some parameters such as ratio of specific heat c_p and γ in Eqs. (13–15) were assumed constant.

The root mean square deviation (RMS) was calculated for each point to assess the goodness of fit of the model to the experimental data. For mass flow, the average deviation is 1.6%, while for the efficiency, the average deviation is 0.61% over the entire simulation range. In addition, the uncertainty in the experimental efficiency (η_t) is illustrated in Fig. 8b. The uncertainties in efficiency vary greatly at different velocity ratios. This is due to the contribution of low torque measurement at maximum velocity ratio [36]. This result indicates that the CFD numerical results consistently agree with the experimental results and the model can be confidently used for further studies.

Comparison of turbine performance analysis

In this work, four-volute configurations are studied under steady flow conditions at a turbine speed of 30,000 RPM and the key performance parameters are recorded**.** All four-volute configurations are designed with a constant volute *A*/*r* ratio in order to provide a consistent basis for comparison. The influence of volute aspect ratio on turbine performance parameters is shown in Fig. 9. Figure 9a shows that all volute configurations capture both the trend and magnitude of the mass flow parameter (MFP) as a function of pressure ratio compared to the baseline simulation (see Fig. 8a). For the

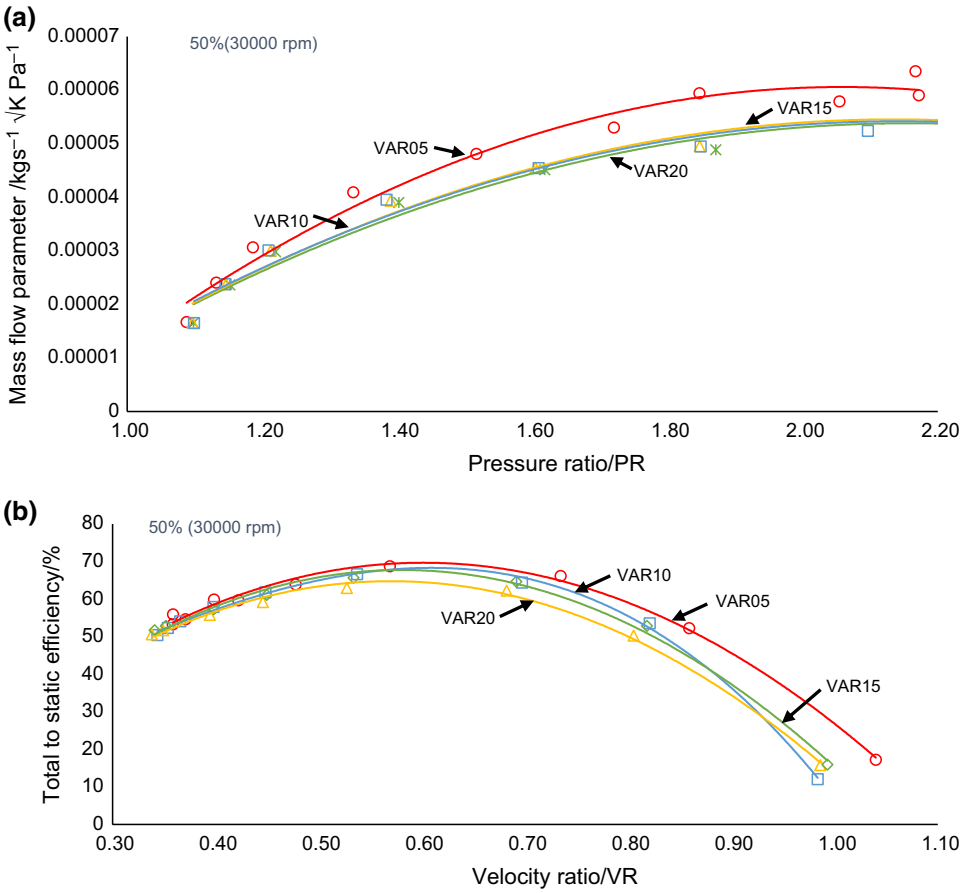

Fig. 9 Comparison among volute aspect ratio towards the steady turbine performance map of **a** mass flow parameter against pressure ratio and **b** efficiency against velocity ratio

same pressure ratio, the MFP for the smaller VAR is higher than that for the larger VAR which agrees with the findings of [20]. As the volute aspect ratio was maintained at a constant *A*/*r,* the maximum flow parameter is expected to remain constant, i.e. independent of the aspect ratio. The results show, however, for VAR05 the MFP is higher than for the other cases, which do maintain a constant MFP. This is consistent with the findings of [20] which suggest that maintaining volute *A*/*r* did not ensure a constant MFP.

Figure 9b shows the comparison of four-volute geometries on total-to-static efficiency which again matches the trend from the experimental work, Fig. 8b. The efficiency curves for each volute in the higher energy region (at low velocity ratio) are close to one another but show a significant difference at the higher velocity ratios. The maximum efficiency is achieved by VAR05 with a peak efficiency of 74.05% compared to 71.21% for VAR10, 71.20% for VAR15 and 70.06% for VAR20. These steady CFD results imply that the smaller volute aspect ratio (VAR) leads to higher turbine performance with less pressure resulting in higher pressure ratio acting on the turbine rotor. The lower VAR also has a higher efficiency over a wider range of velocity ratio. Table 3 summarizes the turbine peak efficiency and the corresponding velocity ratio for the different volutes. It is worth noting that both the peak efficiency and maximum velocity ratio reduce with increasing aspect ratio. In theory, lower velocity region is associated with a higher-pressure region that translates to the improved turbine performance. However, from the current steady analysis, there does not seem to be any clear relation between the variations in volute aspect ratio and the peak efficiency although it seems that VAR05, the smallest aspect ratio, obtained the highest peak efficiency at a higher peak velocity ratio compared to the other three volutes. To understand this, further analysis of the flow field behaviour in the turbine and unsteady flow is required.

Table 3 Turbine peak efficiency and the corresponding velocity ratio for different volute at 50% equivalent speed

Volute	η_{peak}	$VR_{\eta peak}$
YAR05	0.7405	0.6
VAR10	0.7121	0.56
VAR15	0.712	0.56
VAR20	0.7006	0.56
Baseline	0.73	0.58

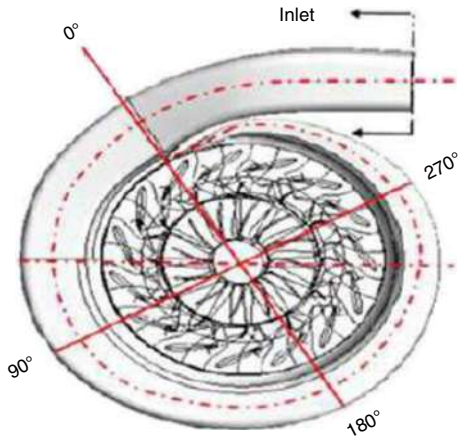

Fig. 10 Selective position of 0°, 90°, 180° and 270° cross-sectional plane in volute

Static pressure and velocity distribution

In order to further understand the factors affecting the flow characteristic within the volute passage, a steady CFD method is employed for the detailed flow structure analysis upstream of the turbine rotor. For this study, the speed of 30,000 rpm and a pressure ratio of approximately 1.3 are chosen as this represents the peak turbine performance. Therefore, the analysis represents the flow field behaviour at the optimum steady-state operating conditions. Analyses of the flow field within the turbine volute (at 50% span) are made at four different azimuth angles (0°, 90°, 180° and 270°) (see Fig. 10). Typical flow profiles in terms of pressure and velocity contours in the volute cross section are shown in Fig. 11 and 12, respectively, for VAR20. It may be seen that the static pressure is distributed in a radial direction and the pressure drops into smaller values as the flow turns towards volute outlet in the most circumferential position. The pressure reduced gradually towards the volute exit in a relatively uniform manner. The flow within the volute stage generally accelerates circumferentially (due to the reduction of the radial distance of the volute centroid to the centre of rotation) and radially as it moves towards the volute outlet. The velocity contours at each volute cross section indicate that the flow accelerates almost radially. This behaviour demonstrates that the flow distribution in the volute is not influenced by the downstream geometry but depends on the design of the volute.

Secondary flow field analysis

In a mixed flow radial turbine, the fluid undergoes a significant radius change as the flow distributes around the annulus periphery of the turbine volute and turns towards the rotor while retaining a large-scale swirl component of velocity. The complexities of the volute geometry induce the development of secondary flow, hence resulting in inefficiencies in the turbine performance. In addition, emerging vorticity in

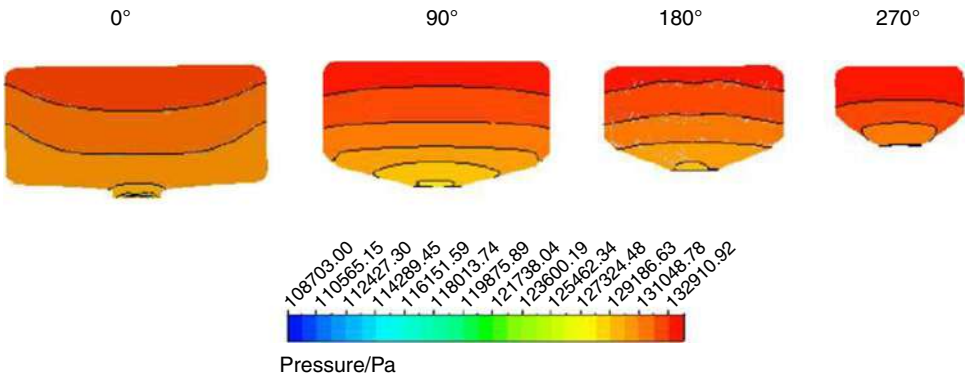

Fig. 11 Pressure contours at different azimuth angles of volute VAR20

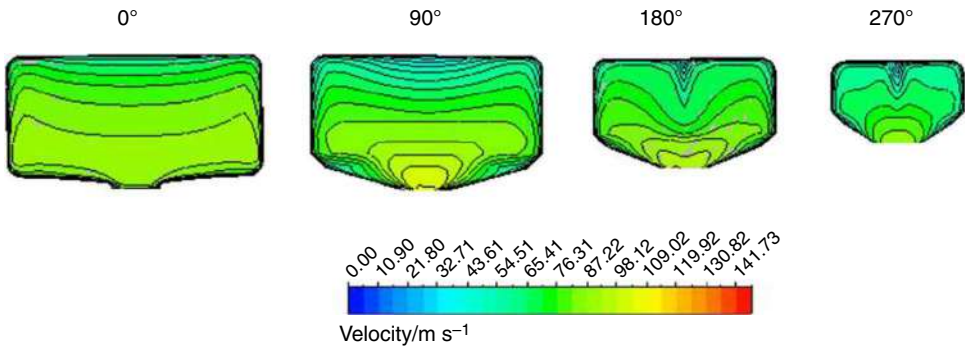

Fig. 12 Velocity contours at different azimuth angles of volute VAR20

a streamline flow, due to centrifugal force generated by the curvature of the volute, increases flow resistance resulting in higher pressure drop along the periphery of the volute. This results in less energy for torque production leading to a reduction in turbine performance.

In an effort to understand the influence of aspect ratio on volute internal flow structure, steady flow structure characteristics of the flow field within the turbine stage are analysed under different operating conditions, as given in Table 1. To demonstrate the changes in flow structure from volute inlet to volute exit, the radial and circumferential velocities are plotted and as a function of dimensionless spanwise distance *X*/*B* from hub to shroud volute wall at a constant radius as defined in Fig. 13.

Figure 14 shows streamlines and contours of radial velocity at four planes around the volute for each volute geometry at the optimum design condition at a turbine speed of 30,000 rpm. The presence of vortex structures is identified in volutes with a larger aspect ratio. It may been seen that as the flow accelerates towards the cross-sectional plane, the topology and size of vortices increase at different locations. Initially, a small "corner vortices" pattern is formed approximately at the top of radius ratio ($r/R = 1$) of the 90° cross-sectional plane for volutes VAR15 and VAR20. The vortices then migrate closer to the centre plane of symmetry (approximately at the radius ratio ($r/R = 0.5$) of the 180° cross section for both volutes. At this stage, the vortices have has become bigger and show a strong secondary flow structure. It is believed that the radial pressure gradient causes the migration of vortices (see Fig. 14a). In this study, the volute cross section is symmetrical and rectangular. In contrast, the presence of vortices for an unsymmetrical rectangular cross section by [19] and a circular cross section by [20] were found in different planes with different topologies. Figure 14b shows that the flow of radial velocity is almost uniform at 0° cross-sectional plane for all volutes. However, as the flow accelerates over the 90°, 180°, and 270° cross-sectional planes, the change in through velocity is found to turn in the parallel to the plane wall which is thought to be due the curvature of the volute passage. It is also observed that as the through velocity changes, the radial velocity parallel to the plane increases as the flow moves to the volute exit. At this point, secondary swirling flows are beginning to develop at the top of all volutes cross section.

For volutes VAR05 and VAR10, the flow becomes more uniform as it moves towards the exit. Furthermore, the radial pressure gradient across the volute cross section did not appear to influence the flow structures significantly [31]; as a result, no vortex structures are apparent in the cross sections for VAR05 and VAR10 at this optimum design condition. In contrast, the streamline shows strong secondary flow over the 0°cross-sectional plane for volutes VAR15 and VAR20. However, this behaviour clearly disappeared when flow moving after the 180° cross-sectional plane, no vortex was developed in all volute geometries albeit the variation in radial velocity across the plane still exists. It is apparent that

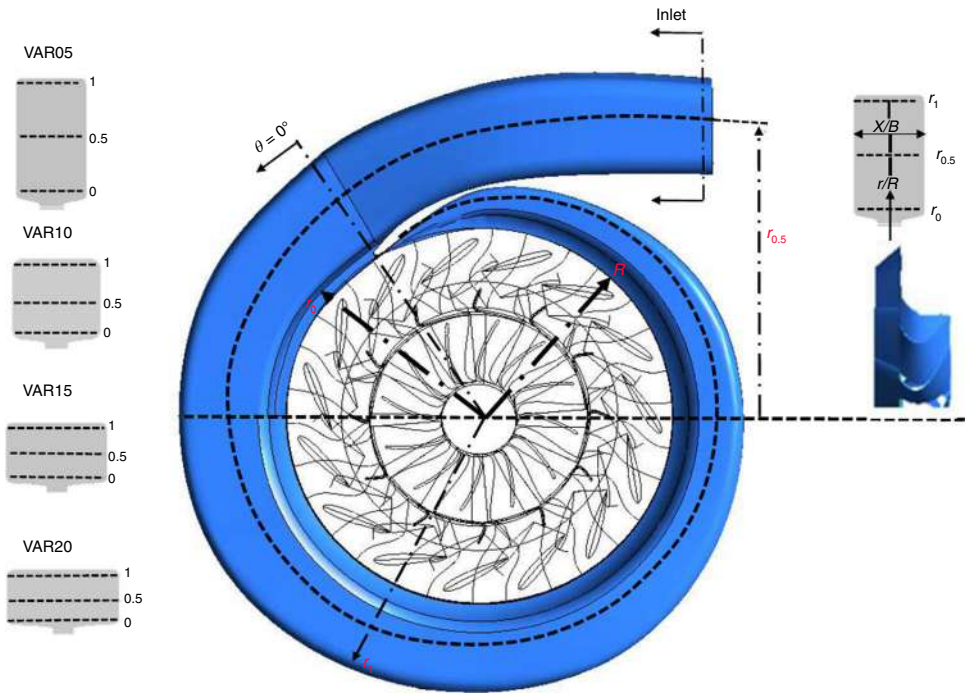

Fig. 13 Position of radius ratio (r/R) in spanwise distance on each volute cross section

* r_n = Radius of volute cross section to rotational axis (m)

* R = Radius of volute discharge to rotational axis (m)

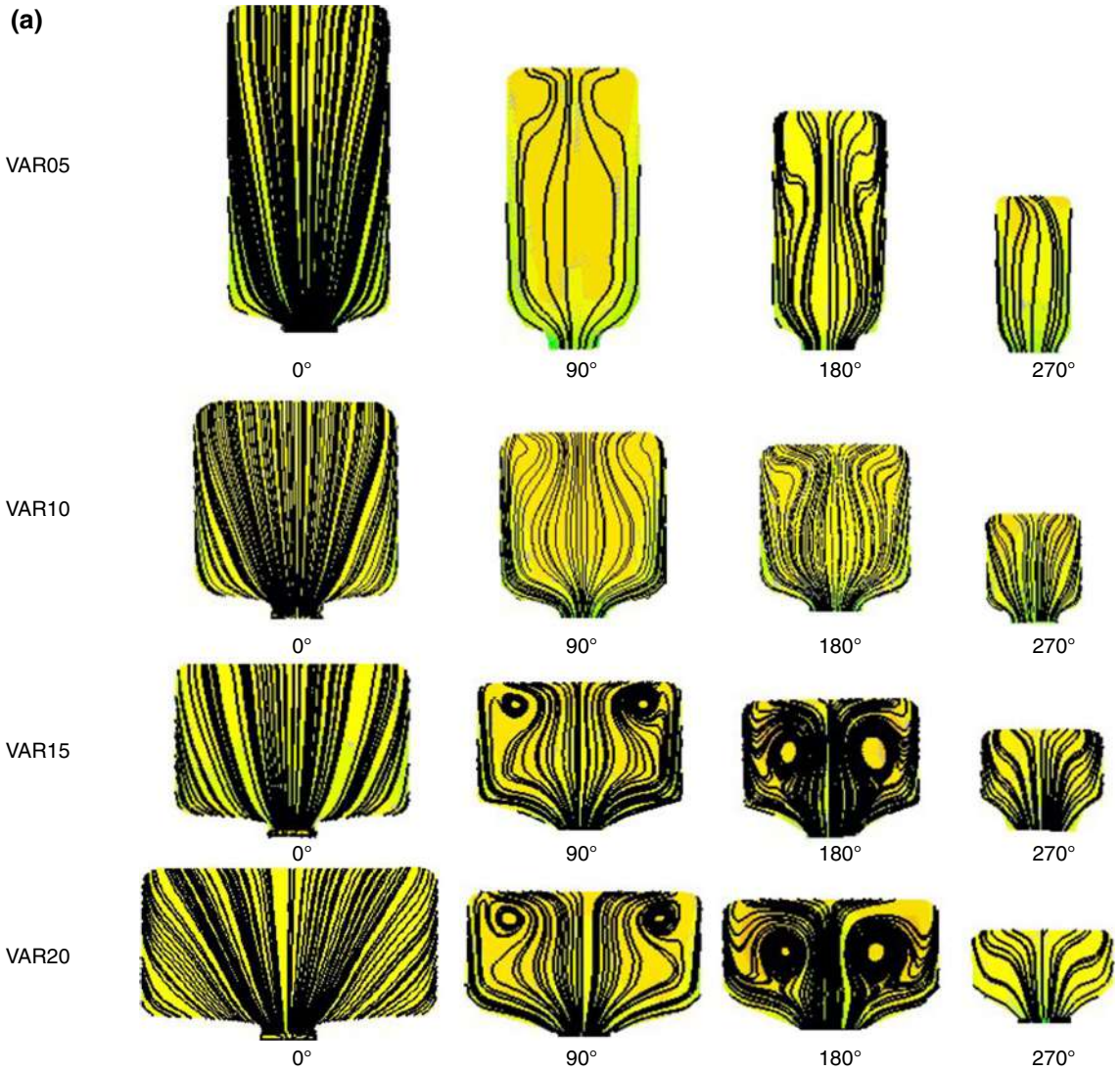

Fig. 14 Plot of **a** streamline and **b** radial velocity contour across the volute stage at mass flow 0.3 kg s^{-1}, (30 K rpm)

the volute geometry directly influences the centrifugal body forces that affect primary streamwise flow. At the optimum design condition, a larger volute aspect ratio intensifies this effect creating more vigorous secondary fluid motion such as the presence of vorticity in the volute region.

The development of the apparent of vortex core in the volute VAR20 is presented in Fig. 15. The flow parameters profiles are obtained at constant radius ratios of 1 and 0.5. For all the plots in Fig. 15, the right and left side corresponded to the shroud and hub side of the volute, respectively. As indicated earlier, the vortices were found at two different locations. It is seen that the "corner vortex" developed at the top ($r/R = 1$) of the 90°plane which is near to volute edge VAR20 (see Fig. 15d). Figure 15a shows that the reduction of the pressure occurs towards the midspan of the volute cross section. Based on the radial velocities (see Fig. 15b), there seems to be a low momentum in the centre of the vortex, $x/b = 0.2$ and $x/b = 0.8$, respectively. The appearance of the "corner vortex" structure indicates higher flow loss in the vortex region. At radius ratio = 0.5 ($r/R = 0.5$) in the 90°plane, the trend of pressure gradients is similar, however, to the magnitude of primary flow distortion which is reduced, while the vortices remain apparent in the upper corners of the volute. This again shows that the flow structure is not influenced by the radial pressure gradient that occurs across volute from inlet to outlet. The volute cross-sectional area reduces as the azimuth angle increases. It is considered that this reduction in area results in the radial pressure gradient affecting a larger proportion of the cross-sectional area, thereby migrating the vortex to the centre of the 180°plane of symmetry (at a radius ratio of approximately 0.5 ($r/R = 0.5$)). Furthermore, the strong downward

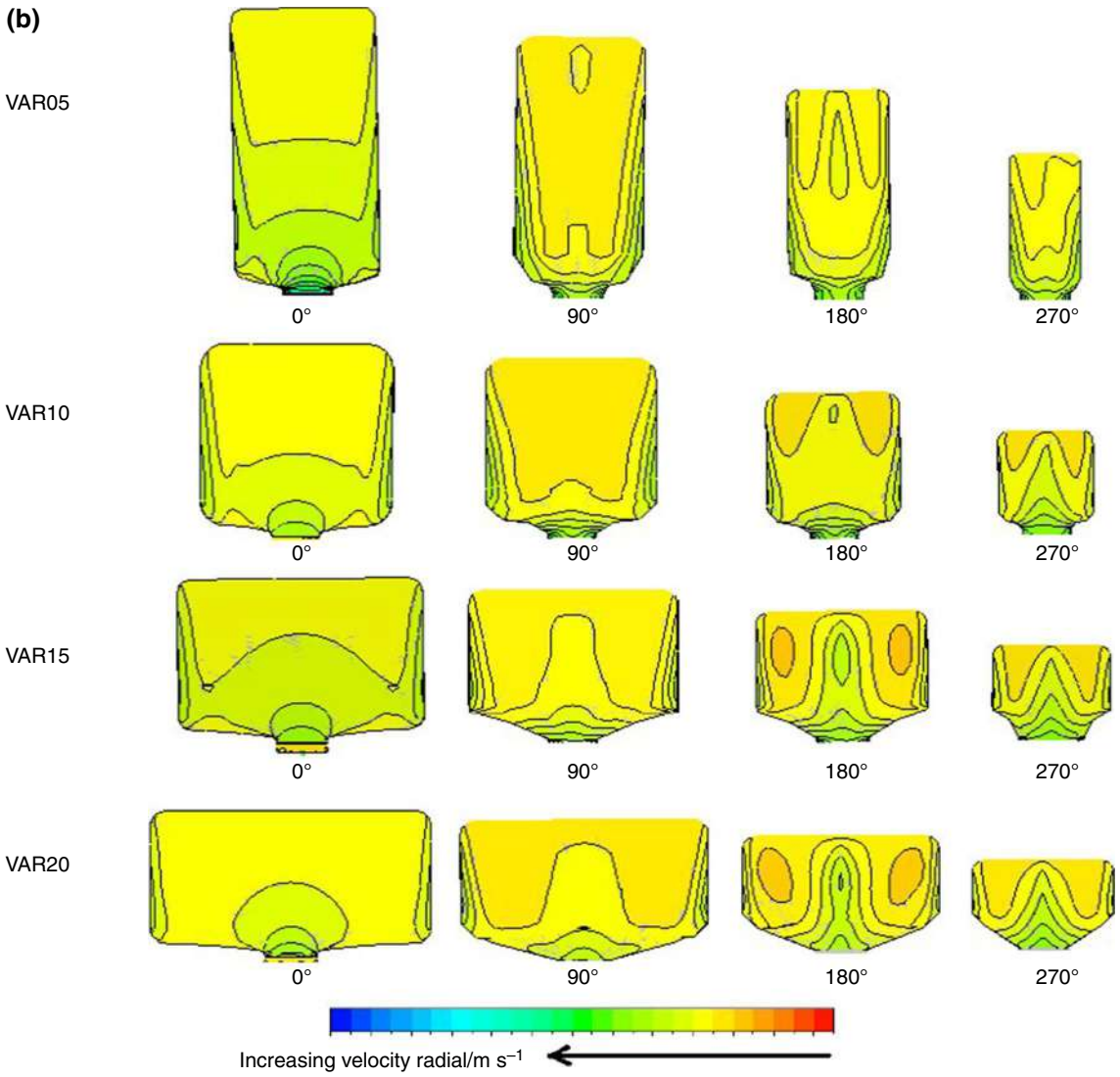

Fig. 14 (continued)

flow into the volute exit has transported low momentum flow from the corner of volute towards the centre of the plane of symmetry [31]. Figure 15b, c illustrates the detail of the radial fluid velocity in the volute passage. This shows that the radial velocity profiles at $r/R = 1$ are non-uniform as the flow accelerates towards the plane of cross sections 90° and 180°. As flow moves down to $r/R = 0.5$, the magnitude of the radial velocity increases towards the centre of the plane resulting in severe spanwise flow distortion. In addition, the radial velocity profiles show tangential flow towards hub and shroud of the volute wall, rat spanwise distance $X/B \leq 0.2$ and $X/B \geq 0.8$, respectively, corresponding to the Dean effect [37]. By its nature, the vane has a shorter hub than its shroud and the flow acceleration appears to impact the flow structure on hub and shroud of the volute wall. An interesting point has been made in this observation that the change in flow angle at the shroud is greater than at the hub (see Fig. 15d, e) which show that a stronger magnitude of vortex structure is developed on the shroud side.

Mass flow effect

Figures 16 and 17 show weak deflection of streamwise flow at the lower mass flow rate changing to strong deflection both with position and increasing mass flow. At stronger deflections of primary streamwise flow, separation occurs resulting in the generation of stronger vortex structures within the volute cross sections especially at higher mass flow rates. These variations of the flow field structures may result in a lack of continuity in the turbine performance curve. For the two volutes, VAR05 and VAR15, shown in Figs. 16 and 17, respectively, the lower velocities at the low

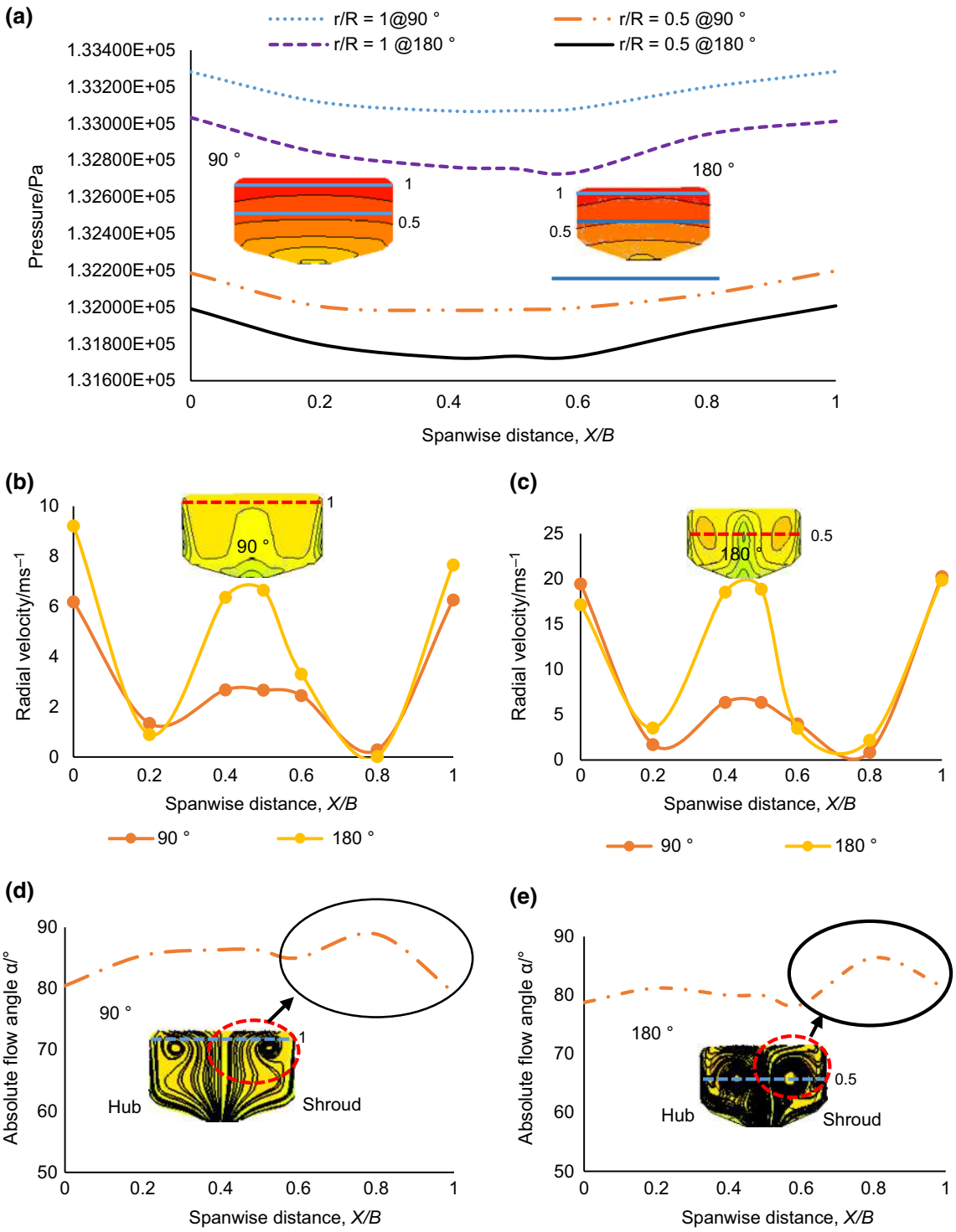

Fig. 15 The development of the apparent of vortex core in the volute VAR20. Graph **a** pressure at radius ratio ($r/R=1$) and ($r/R=0.5$) at 90° and 180° plane; **b** and **c** radial velocity at ($r/R=1$) and ($r/R=0.5$), respectively, at 90° and 180° plane; **d** and **e** absolute flow angles at ($r/R=1$) and ($r/R=0.5$), respectively, at 90° and 180° plane

mass flow lead to the development of positive radial fluid pressure field in the volute cross section, thus inducing fluid motion from the top of volute cross section to volute exit.

As more fluid enters the volute at the design mass flow rate, the fluid motion becomes stronger and there is a larger the radial pressure field in both designs. Meanwhile, at a

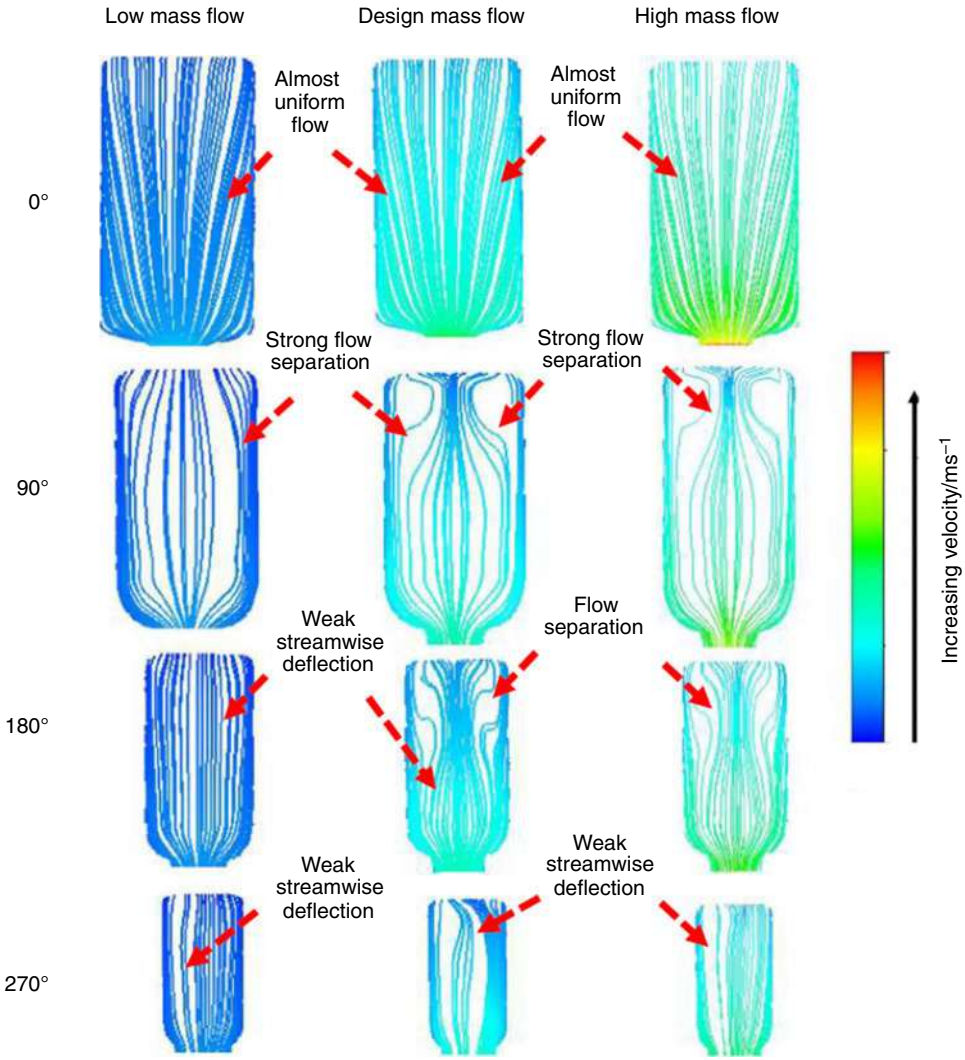

Fig. 16 Volute VAR05 flow structure

mass flow higher than the design rate, significantly stronger fluid motion is seen with a larger fluid velocity and amplified radial pressure field, Figs. 16 and 17. The combination of these two elements of larger radial pressure and the viscous effect inhibit fluid motion forming a stagnation region in volute VAR15. In this analysis, the presence of vortex structures in the stagnation region has been identified to occur only in volute VAR15 and not in volute VAR05 albeit the variation in radial velocity across the plane still exists as shown in Fig. 20. The vortices that formed were observed to have different sizes and topology at different locations across these volute cross sections, Fig. 17. A small "corner vortices" pattern (labelled in Fig. 17) was formed approximately at the top of 90° cross-sectional plane of volute VAR15, while, due to the flow towards the volute exit, the vortices migrated closer to the centre plane of symmetry at the 180° volute cross section. A strong secondary flow structure was captured at this particular cross section, and the vortices appear to be larger size.

The contour distributions of the static pressure and total pressure across the volute VAR15 cross-sectional plane at 180º are shown in Figs. 18 and 19, respectively. The static pressure is distributed in a radial direction, and the pressure drop becomes smaller as the flow turns towards the volute outlet in the most circumferential position. The appearance of vortex structures in the centre plane of symmetry of 180° volute cross section at design and high mass flow rates indicates that a low momentum flow is entering vortex region as a result of the static pressure gradient. Therefore, the total pressure is higher in the volute cross section centre (feature A) than near the wall, and this is shown in Fig. 19. However, as the flow reaches the volute exit, the magnitude of the total pressure decreases for all operating conditions.

Figures 20 and 21 show contours of radial velocity at four-volute cross-sectional planes around the volute for both geometries at three different mass flow rates. It was observed that in all operating conditions, the radial flow velocity was almost uniform at 0° cross-sectional plane for both volutes.

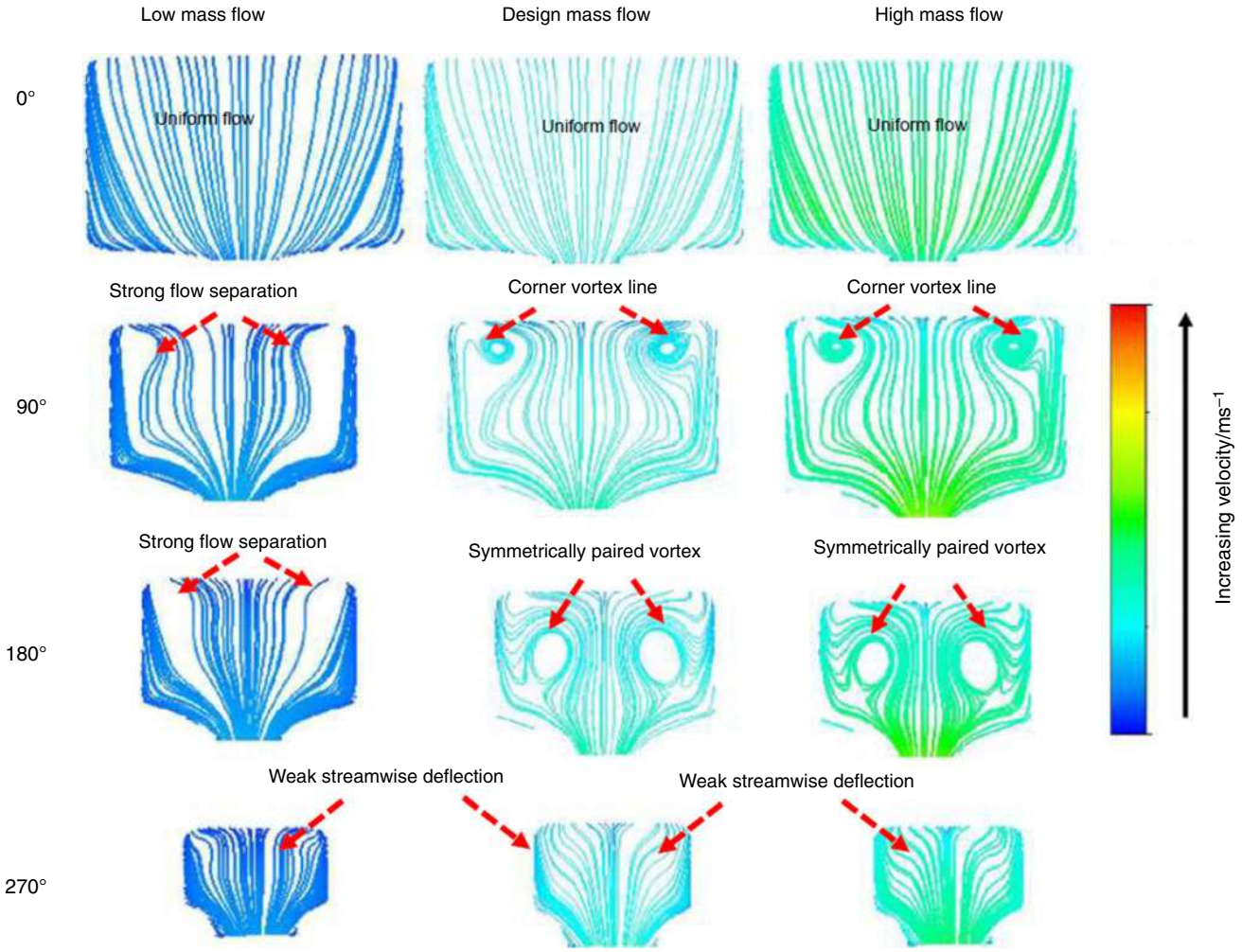

Fig. 17 Volute VAR15 flow structure

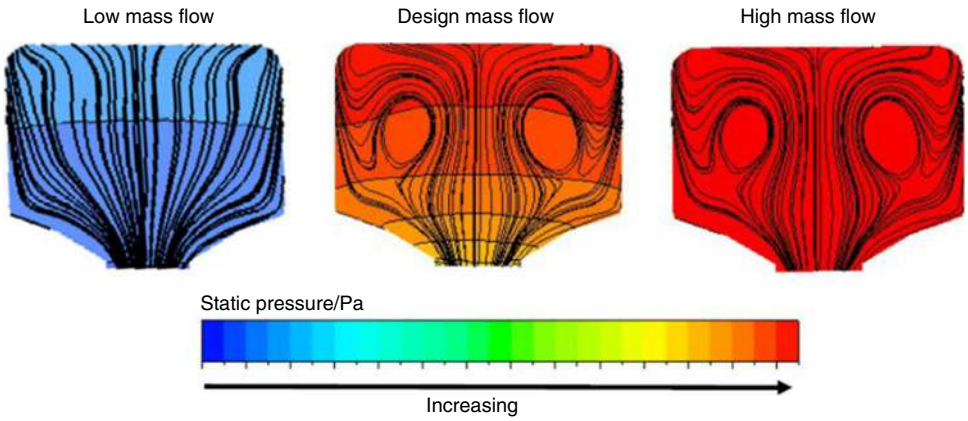

Fig. 18 Static pressure distribution at 180° cross section of volute VAR15 at three different operating conditions

However, changes in through velocity are seen over the other plane cross sections for both volutes, as the flow turns parallel to the plane wall due to the curvature of the volute.

The maximum radial velocity was found to occur parallel to the plane wall (feature B) and becomes larger in magnitude as flow moves down to volute discharge. This condition results in the onset of flow distortion at the top of both volute cross sections; however, it may be seen that for volute VAR05 the flow is more uniform towards the volute exit compared to volute VAR15.

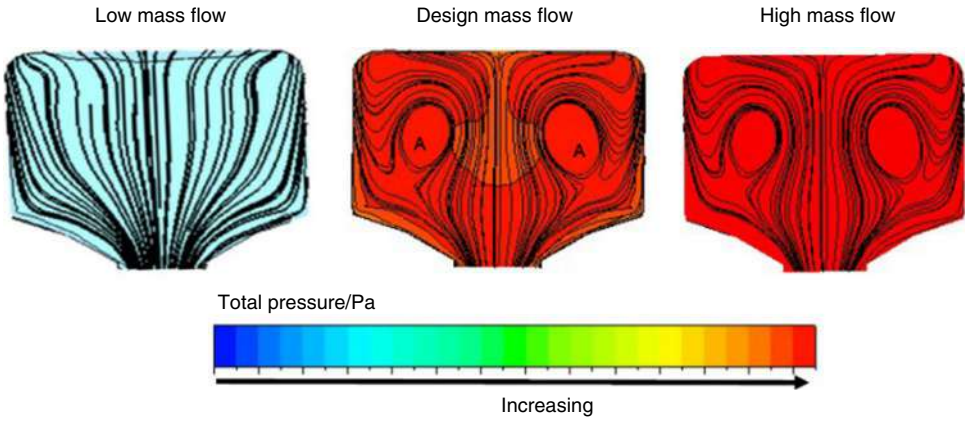

Fig. 19 Total pressure distribution at 180° cross section of volute VAR15 three different operating conditions

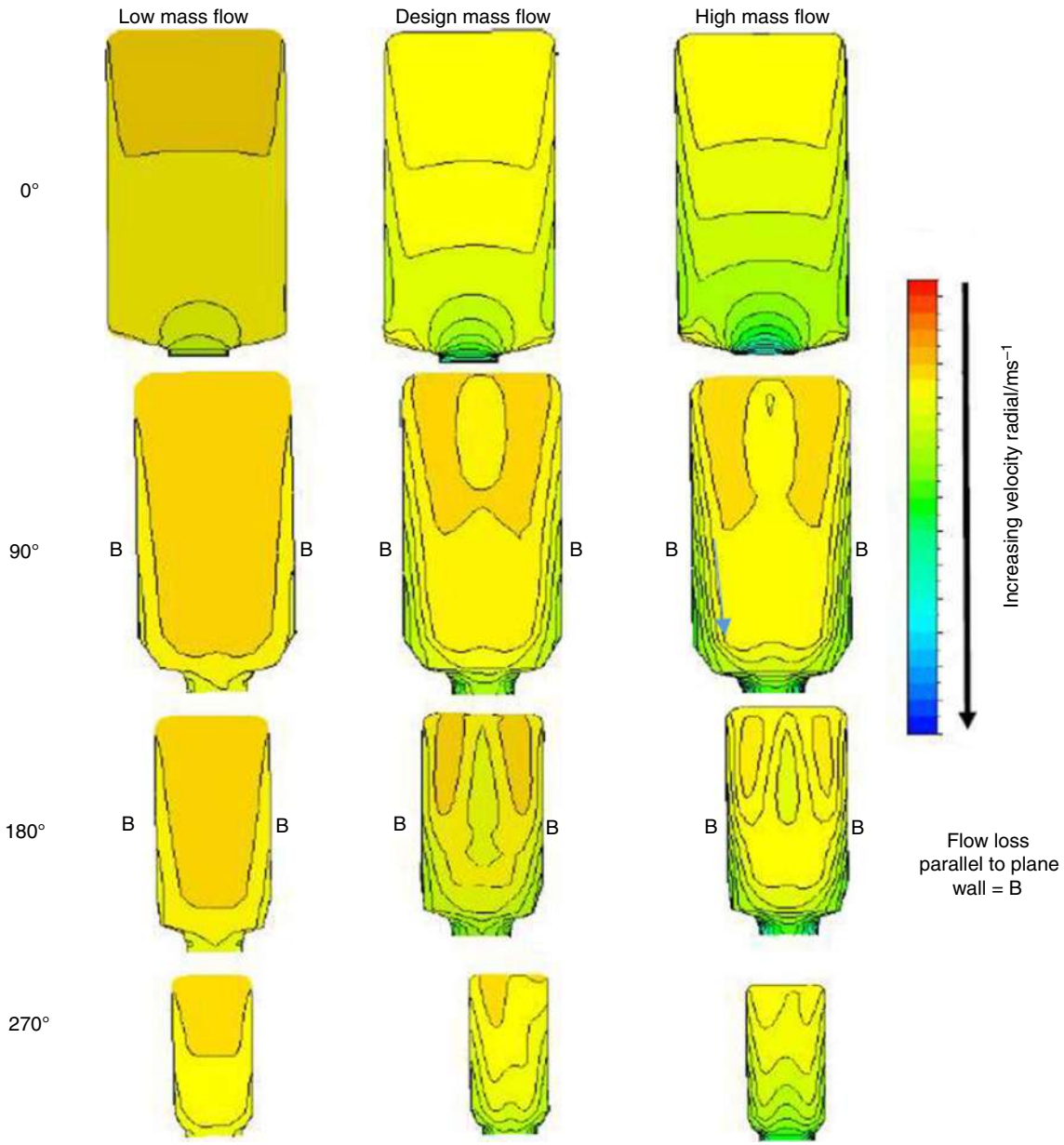

Fig. 20 Radial velocity contour across volute VAR05 cross section at three different operating conditions

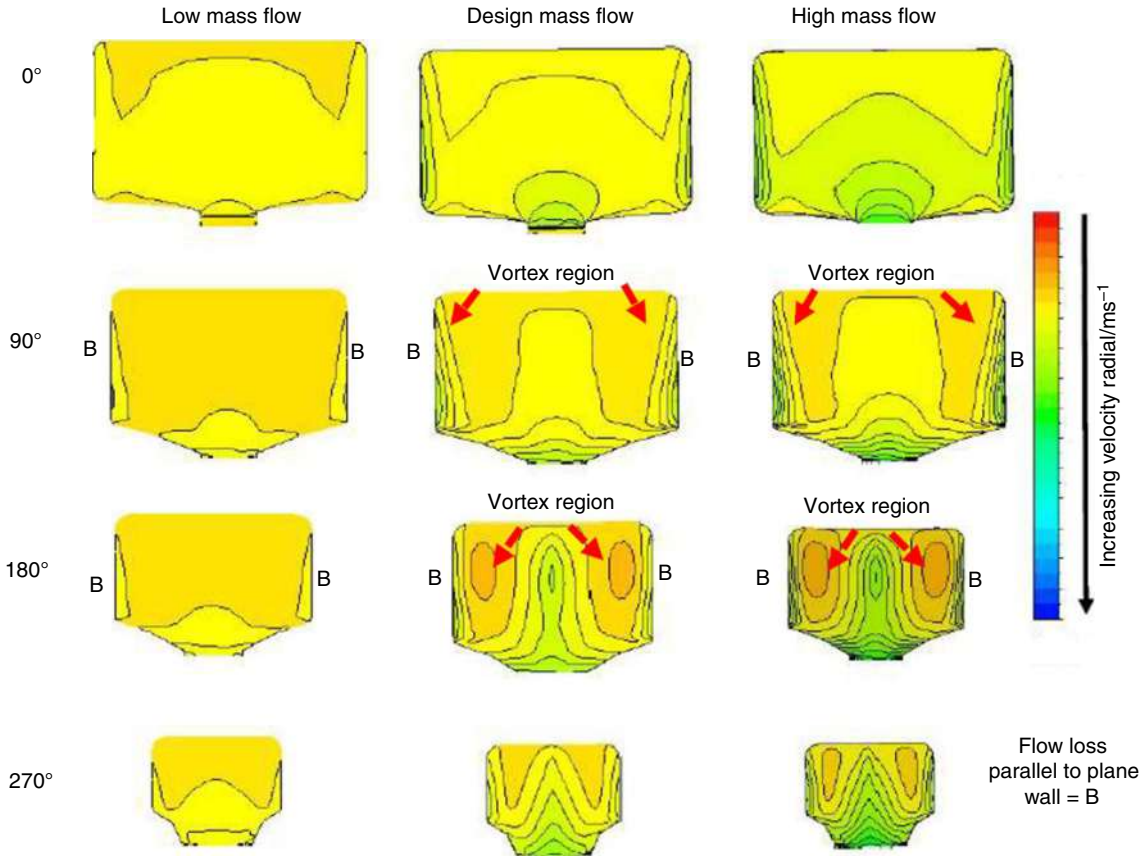

Fig. 21 Radial velocity contour across volute VAR15 cross section at three different operating conditions

Consistent with [31], for volute VAR05 the pressure gradient across the volute cross section did not appear to influence the flow structures significantly with no vortex structures seen under all operating conditions. In contrast for VAR15, as indicated in Fig. 17, the streamlines show strong secondary flow development over the 0° cross-sectional plane at all operating conditions**.** Interestingly, the vortex regions are clearly seen in the radial velocity contours, Fig. 20. It is apparent that in Fig. 17 the topology and size of vortices in volute VAR15 cross-sectional planes are almost identical in the design and higher mass flow rates conditions. At the higher mass flow, however, the vortices are more distinct and have a stronger structure. In addition, higher velocities and high pressure losses are recorded at the larger mass flow rate as flow moves towards the sharp corner of the volute discharged [30]. At the larger mass flow rate, the combination of larger radial pressure gradient and viscous effects strongly inhibits fluid flow causing the formation of a stagnant flow region. At this point (see Fig. 17)**,** the fluid flow direction reverses and forms a weak local recirculation flow and secondary couple vortex flow structure in stagnant flow region, and this effect is attributed to Dean [37].

The presence of a secondary flow structure is always associated with energy losses [24]. At the design mass flow rate, secondary flow structures were not observed for both volutes resulting in continuity of the turbine performance curve enhancing its overall performance. At low mass flow, however, different mechanisms are observed. A weak almost uniformly constant radial flow velocity (see Figs. 20 and 21) is seen at circumferential positions in both volute geometries. In addition, as indicated in discussion of Fig. 18, at low mass flow, low-pressure magnitude is recorded as the flow moves towards the circumferential curvature of the volute discharge. Nevertheless, in both volute aspect ratios, at all different operating conditions, as flow moves over the remaining 270° of volute cross section, no vortex structure is seen in both volute geometries albeit the variation in radial velocity across the plane still exists. It is apparent that the volute geometry directly influences the centrifugal body forces that affect primary streamwise flow motion.

A larger volute aspect ratio may create more vigorous secondary fluid motion resulting in vorticity in the volute region. As noted earlier, the variations in the flow field structures in volute passage result in poor turbine performance. In addition to the parameter study, extensive analyses of the

complex flow structure in the volute were carried out under different operating conditions. The flow parameters of absolute flow angle are presented as a function of dimensionless spanwise distance, *X*/*B* from hub to shroud volute wall (see Fig. 22). The absolute flow angles profiles are graphically demonstrated at two locations spanwise distance, *X*/*B* denoted as (feature C at 90°) and (feature D at 180°), respectively. The volute passage absolute flow angle is defined as the angle of the flow from the radial direction (see Fig. 22). At low mass flow rate, the absolute flow angles were observed to be the greatest uniform of both volute geometry of all three mass flow rates analysis. As seen in Figs. 23 and 24, the difference between the absolute flow angles profiles of both volutes is small, but greatest fluctuation flow was found at feature D at 180° of volute VAR15 plane.

For each volute, the absolute flow angles, as a function of the dimensionless spanwise distance, X/B, for the 90º and 180º cross-sectional planes, are plotted in Figs. 23 and 24, for three different mass flows. For volute VAR05, Fig. 23 shows that at the 90° and 180° plane positions, there is a significant drop of the flow angle towards the hub and the shroud at spanwise distances $X/B \leq 0.2$ and $X/B \geq 0.8$. Figures 23 and 24 also show non-uniformity of flow at the hub and shroud for all mass flows. For both volutes, the tangential flow angle is uniform for $0.2 \leq X/B \leq 0.8$; however, as the flow increases, the angle becomes less uniform. The rate of drop off of the flow angle is greater in the 90º cross-sectional plane due to the strong flow separation in this (feature C spanwise) section. The results for volute VAR15, Fig. 24, show the similar trends exist for flow angle and flow non-uniformity at the same spanwise locations as in volute VAR05. This flow variation is indicated by the feature D at 180° plane position where the absolute flow angle dropped significantly, by a maximum of 13º at a spanwise distance between 0.2 and 0.6. Due to a reduction in the volute cross-sectional area creating a strong downward flow into the volute exit, transporting momentum flow from the top corner (feature C spanwise) of the volute towards the centre of the plane of symmetry. Moreover, with volute VAR15, non-symmetrical flow angle profiles (see feature D) were found during design higher mass flow rate.

In a parallel study, an important observation was that the flow structure for volute VAR10 exhibited significant deviation at lower and higher pressure ratios. As the mass flow is increased, the deflection of primary streamwise flow becomes stronger, and the radial pressure field is intensified as shown in Fig. 25a, b. As the flow migrates gradually inwards to the volute exit, the secondary flow pattern demonstrates an almost symmetrically paired and counter-rotating vortex (Dean flow pattern) at lower section of the volute cross section (see Fig. 25b). Based on the pressure profiles, these counter-rotating vortices are transporting low momentum boundary layer fluid away from the centre region ($X/B = 0.5$) towards the hub and shroud between $X/B = 0.2$

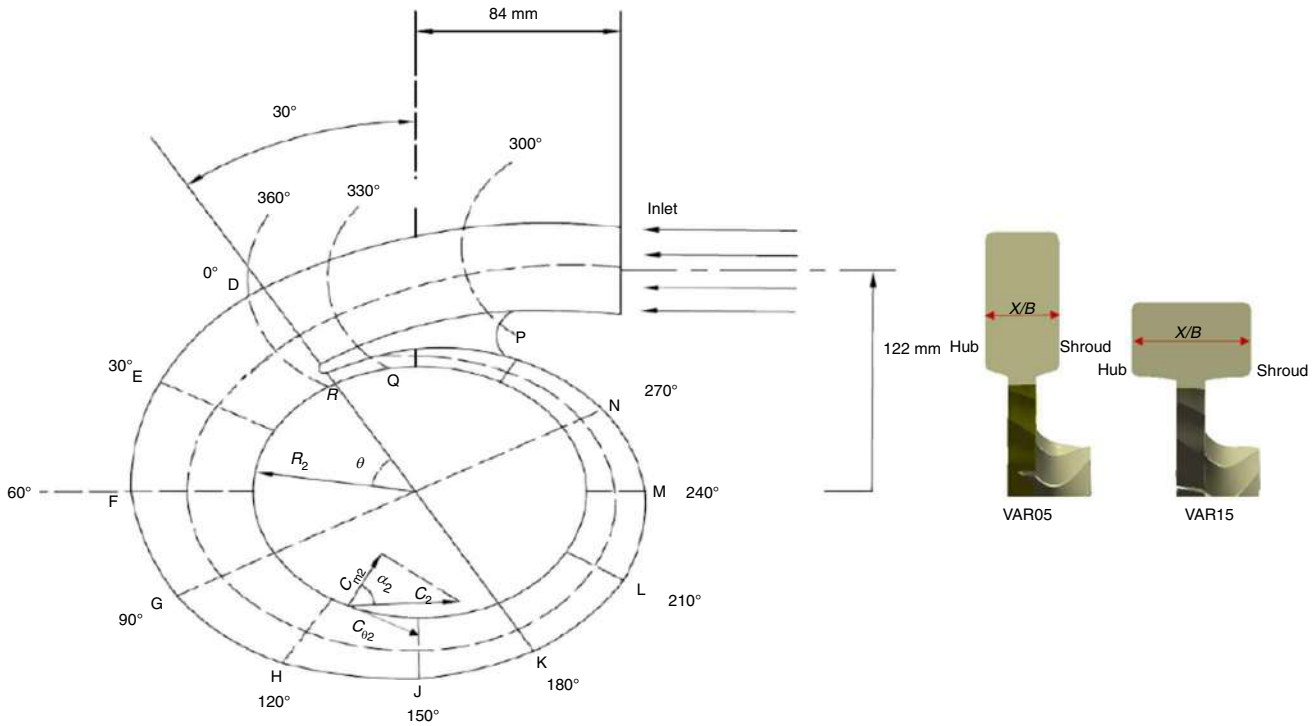

Fig. 22 The volute flow angle (α) direction and dimensionless spanwise distance, *X*/*B* of both volute cross section

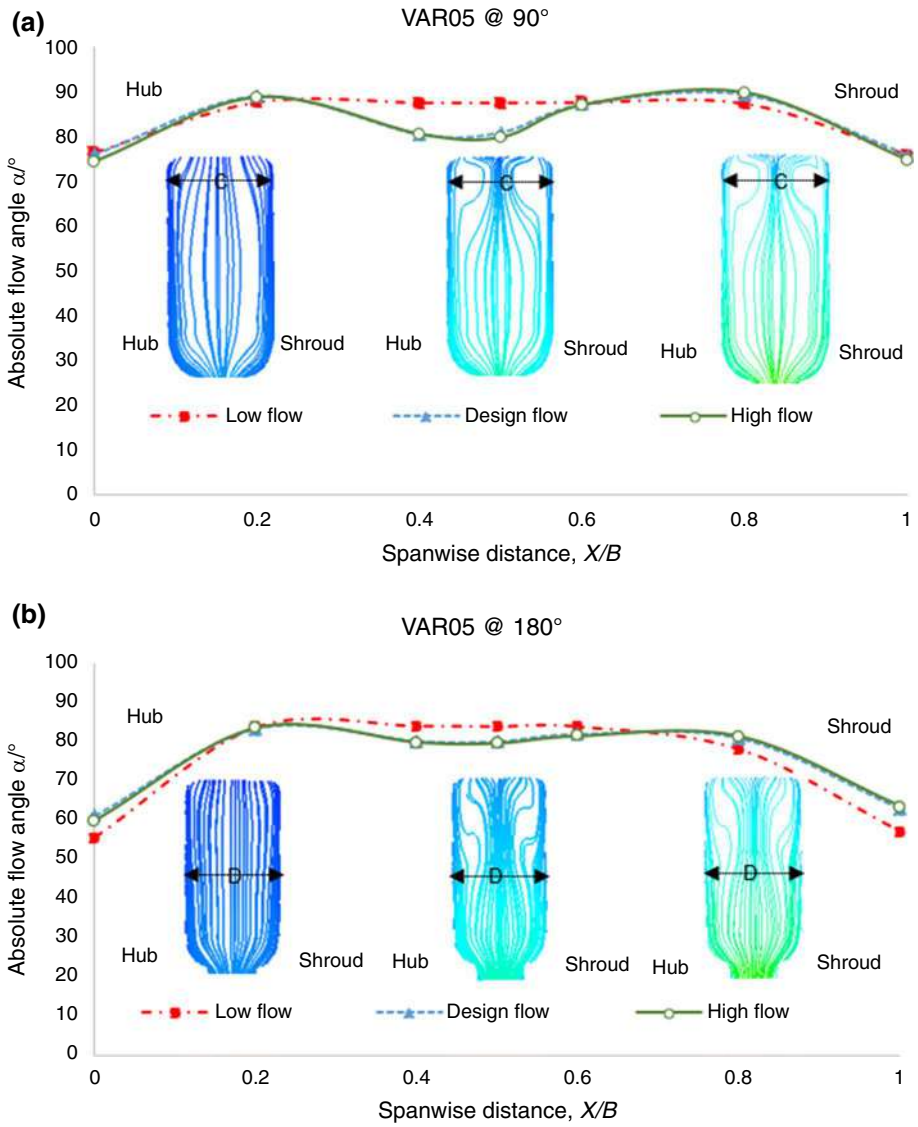

Fig. 23 Comparison of the trend of absolute flow angle distributions on C and D spanwise distance, respectively **a** at 90° and **b** 180° of volute VAR05

and $X/B = 0.6$. However, the strong downward flow into the volute exit causes growth of the boundary layer towards the volute wall side at ($0.2 < X/B > 0.8$). In addition, it may be seen that increasing the pressure ratio results in higher velocities towards the volute exit (see Fig. 25c). Although the volute geometry is symmetrical, the plot of the absolute flow angle across the shroud demonstrates more asymmetry as the load increases, Fig. 25d. The flow angle dropped to 37° in the shroud region as a result of the stronger vortex structure. The radial velocity profiles Fig. 25e show some interesting features, namely a weak localized swirl streamwise towards the centre lower part of 90° plane position. Consistent with [19], it is apparent that the secondary flow in the volute is enhanced by the higher load, thus resulting in stronger primary streamwise deflection. With the pressure drop towards the centre lower region of the volute cross section, a low radial fluid flow is established around the swirl streamwise deflection resulting in the secondary couple vortex flow structure, Fig. 25e.

Under the steady flow condition, early indications showed that at lower pressure ratios, the free vortex development is satisfactory for the smaller volute aspect ratios of VAR05 and VAR10 at all the positions. Meanwhile, for the volutes with higher aspect ratios, more streamwise flow deflection occurred at certain positions producing vortex structures. This shows good agreement with steady flow the CFD results which demonstrates that smaller aspect ratios result higher turbine performance (see Fig. 8b). As such, this gives an early indication that flow behaviour is greatly influenced by the volute aspect ratio.

However, as the pressure ratio increases (at more than 0.65 kg s^{-1}), the secondary flow in the volute cross section becomes stronger resulting in vortex generation even for volute VAR10. This finding was clearly explained in the

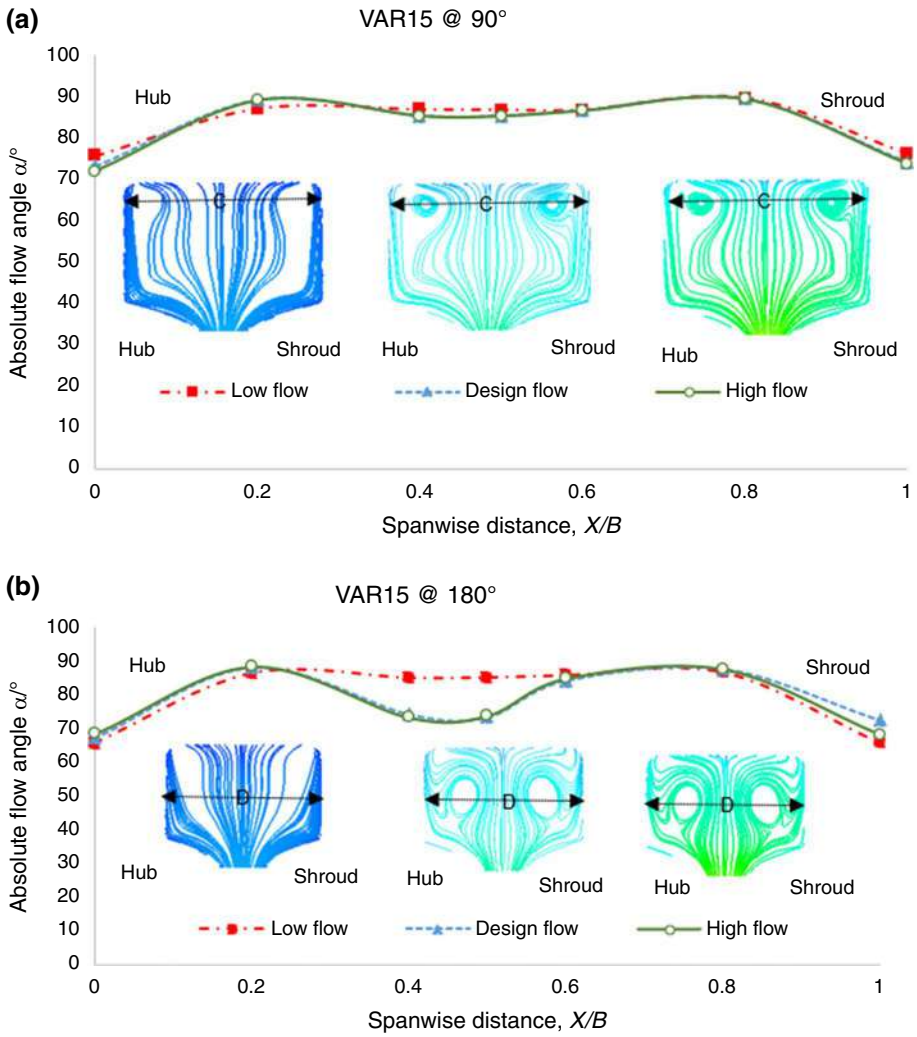

Fig. 24 Comparison of the trend of absolute flow angles distributions along C and D spanwise distance, respectively **a** at 90° and **b** 180° plane of volute VAR15 during low, design and high mass flow rates conditions

work of [37] and [38] who pioneered the work in this field. In conclusion, the flow distribution in the volute is not influenced by the blade geometry downstream but depends on how the design of the volute. This may be better understood by performing unsteady flow analysis and experimental work in the near future.

Flow transition over volute passage

The variation of flow transition over the volute passage of VAR20 is presented in Fig. 26 for radius ratios, r/R as described in Fig. 26, of 1 and 0. Figure 26a (left) shows that the radial velocity profiles at radius ratio ($r/R = 1$) in the inlet (0°plane position) are distributed uniformly; however, as the flow accelerates towards the plane of cross sections 90°, 180°, and 270°, the radial velocity profile become less uniform. Meanwhile, at the lower radius ratio, $r/R = 0$ Fig. 26a (right), the maximum radial velocity is found at the centre and remains less uniform in all volute plane positions. Figure 26a (right) also illustrates the secondary flow effect on the radial fluid velocity in the volute passage. The radial velocity profiles indicate that there is tangential flow towards hub and shroud volute walls, respectively, at spanwise distances $X/B \leq 0.2$ and $X/B \geq 0.8$ corresponding to the Dean effect. Meanwhile, the profiles show a nearly symmetrical distribution with spanwise distance in the region of $0.2 < X/B > 0.8$. In a symmetric distribution, the hub wall side of the distribution is a mirror image of the shroud side of the distribution. The circumferential velocity distribution is shown in Fig. 26b (left); there is an obvious change in the flow structure as the flow moves around the volute. At constant radius ratio, ($r/R = 1$), the magnitude of velocity circumferential decreases towards the plane centre, while at $r/R = 0$, the circumferential velocity increases towards the plane centre, Fig. 26b (right). The greatest variations are in the 90º and 180º planes where vortices are found in the volute cross section. However, at the 0º and 270º planes more uniform velocities are found as there are less secondary flow effects at the inlet and towards the outlet of the volute. Figure 26c shows the absolute flow angle around the

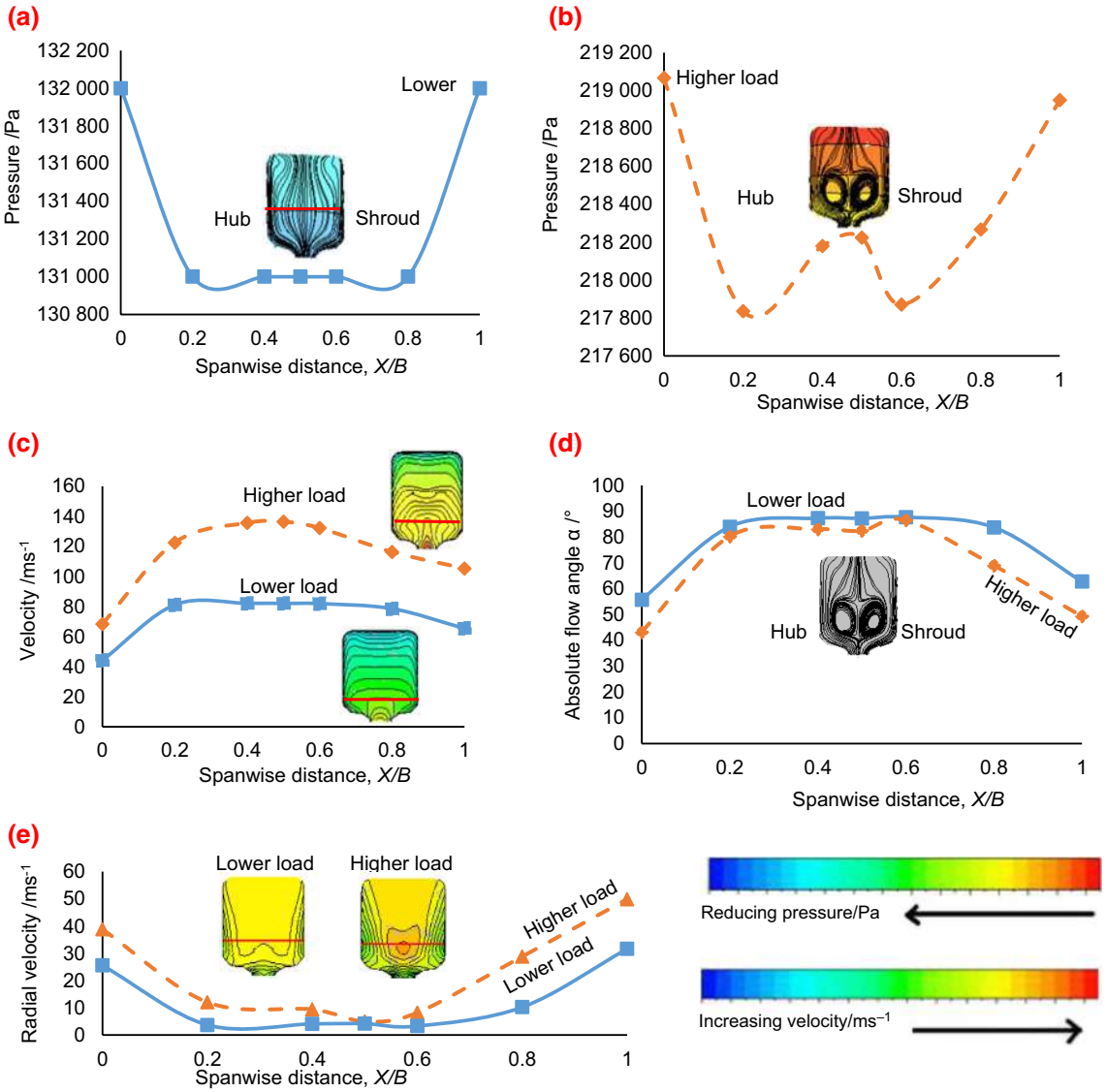

Fig. 25 Comparison of the flow characteristics under lower and higher load for VAR10 at 90°

circumference of the volute at constant radius ratios ($r/R=1$) (left) and ($r/R=0$) (right). At the higher radius ratio, the absolute flow angle was found to be uniform at the volute inlet position compared to the remaining volute plane positions. The absolute flow angle becomes less uniform at the lower radius ratio where significant variations are seen in all planes. It is apparent from Fig. 26c right that the 90° and 180° planes show similar flow angle fluctuations with a maximum variation of 22 degrees, indicating the presence of a vortex in these planes.

Fluctuating velocity

The function of the volute is to uniformly accelerate fluid around the rotor periphery to the desired velocity and flow angle. In this study, the volute cross section is rectangular with rounded corners and since it is symmetrical, the distribution of radial velocity profiles is somewhat symmetrical about the section mid span, $X/B=0.5$ (see Fig. 26a). The data are almost similar in direction and magnitude between spanwise distances, $0 \le X/B \ge 0.5$ and $0.5 \le X/B \ge 1$. The radial velocity variation with azimuth angle is shown in Fig. 27 for the radius ratio $r/R=0$ and for two spanwise distances of $X/B=0.2$ and $X/B=0.5$. Overall, the symmetrical volute cross section causes at the inlet the main radial inflow to occur at the centre of the volute cross section. In all the volute geometries, there is a reduction in radial velocity as the flow reaches the 90° azimuth angle, increasing back as the flow moves around the volute. Except for volute VAR05, the main radial velocity is observed in the

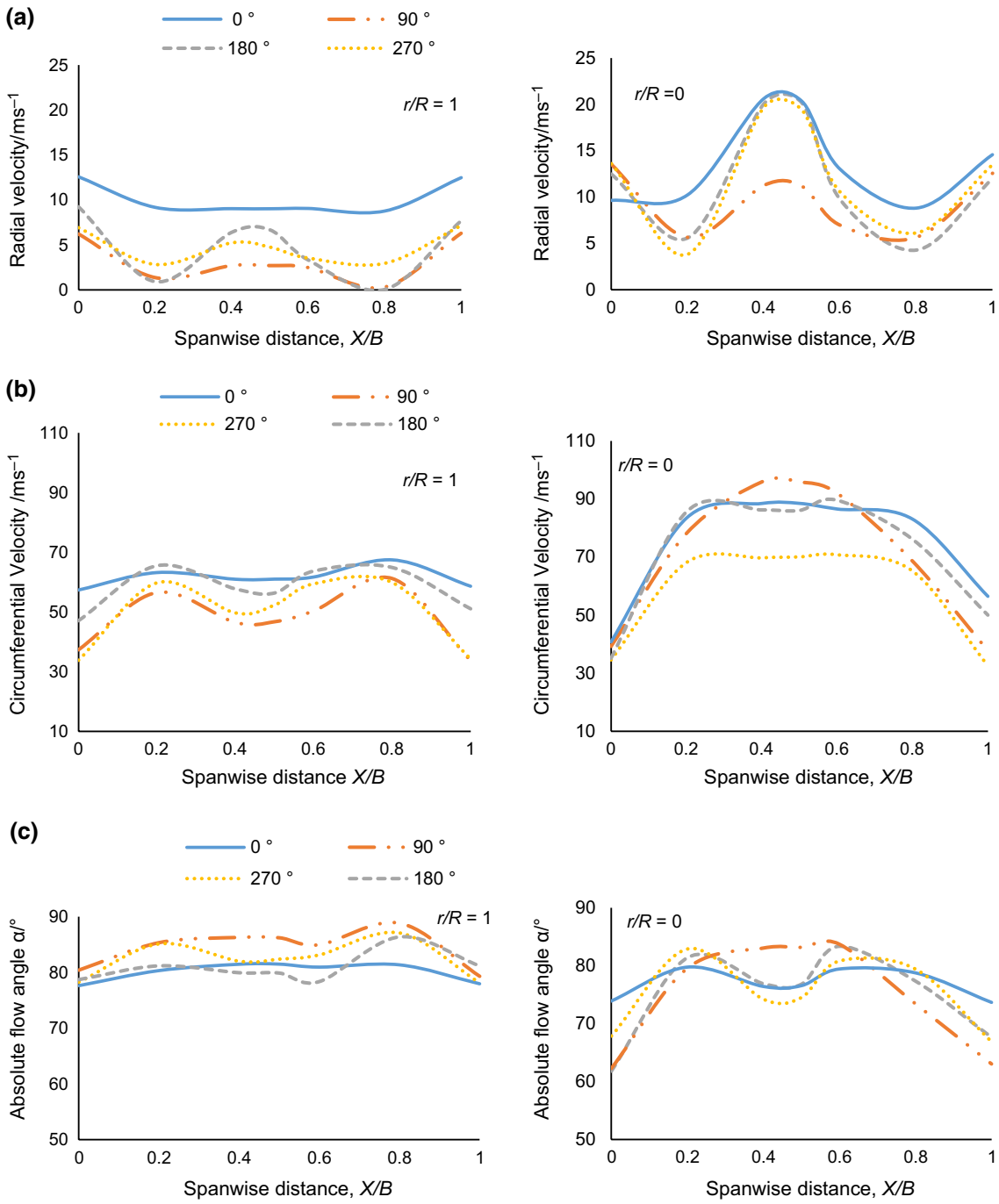

Fig. 26 Volute VAR20 passage **a** radial velocity; **b** circumferential velocity; **c** absolute flow angle at radius ratio ($r/R=1$) (left side) and radius ratio ($r/R=0$) (right side) at 0°, 90°, 180° and 270° position

centre region ($X/B=0.5$) of the volute cross section. However, for volute VAR05, despite having a higher inlet radial velocity, 35 m s^{-1}, compared to the other volutes, as the flow reaches the 90º azimuth angle, the radial velocity at $X/B=0.2$ becomes higher than the centre velocity, $X/B=0.5$, as the flow moves round the circumferential volute. Even though this may be evidence of secondary flow structure developed in this plane for no vortex, no vortex is seen under the current steady flow conditions. Instead, the tangential flow trends occur between the 90° and 180° planes in the cross section of volutes VAR15 and VAR20 corresponding to the Dean effect. Figure 28 shows the development of Dean-like vortices in volute VAR20. The appearance of vortices at 180° volute plane indicates a higher flow loss

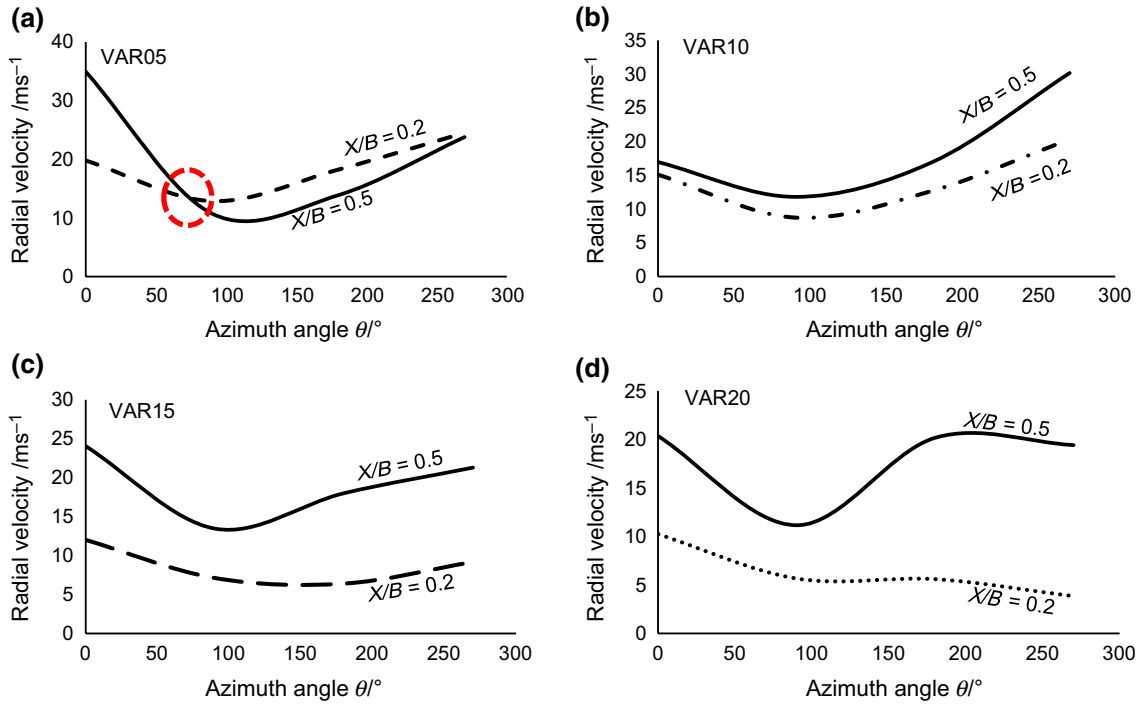

Fig. 27 Radial velocity variation with azimuth angle **a**–**d**

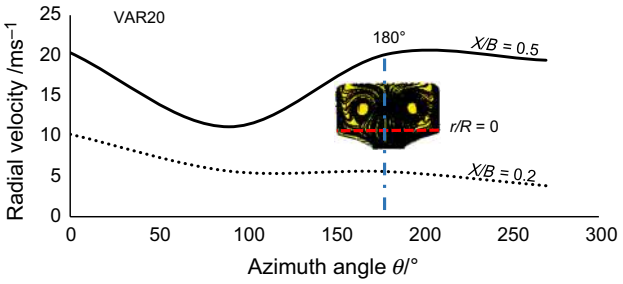

Fig. 28 Dean-like vortex development on volute VAR2

region occurring from the midspan ($X/B = 0.5$) of vortex cross section toward the volute wall region ($X/B = 0.2$). As a consequence, there is a significant drop in the radial velocity profile towards the volute wall, $X/B = 0.2$, as the flow moves round the volute which is not seen in the other volutes. Meanwhile, it is believed that at large value azimuth angles the increasing radial velocity along the centre region ($X/B = 0.5$) is due to the influence of the volute tongue.

Conclusions

This work analysed the effect of volute aspect ratio (VAR) on the secondary flow characteristics of a mixed flow turbine volute at different operating conditions. The flow structures for the four-volute geometries are found to be dependent on the volute aspect ratio (b/h) with greater secondary flow structures occurring at higher aspect ratios. Meanwhile, at higher mass flows, the secondary flow is enhanced resulting in stronger secondary flow development. There are significant differences in the flow profiles for each volute geometry and operating conditions suggesting a strong correlation between the volute geometry and primary streamwise deflection. At the optimum design conditions, at low aspect ratio there is a high continuity in the turbine performance curve. This work may provide a guideline for the analysis downstream of the turbine volute discharge. Future work such as conducting analysis under unsteady conditions is recommended to further understand volute design.

Acknowledgements This research is funded by Ministry of Higher Education, Malaysia, under Fundamental Research Grant Scheme No FRGS/1/2019/TK07/UTM/02/17

Author contribution Amiza Azmi is currently a 4th year PhD student under the supervision of Dr. Muhamad Hasbullah Padzillah, at Universiti Teknologi Malaysia. Amiza is the first author of this paper, which means that the data presented here are the results of her research. Dr. Muhamad Hasbullah Padzillah is the PhD supervisor of Amiza. Dr. Hasbullah is responsible for the general direction of this research and provided valuable input vital to the completion of this paper.

References

1. Ritchie H. Greenhouse gas emissions come. 2020. http://ourworldindata.org/greenhouse-gas. Accessed 18 September 2020.
2. Environmental Protection Agency (EPA). Inventory of U.S. greenhouse gas emissions and sinks. 1990–2018. https://www.epa.gov/ghgemissions. Accessed 13 April 2020.
3. Fakhari AH, Shafaghat R, Jahanian O, Ezoji H, Motallebi Hasankola SS. Numerical simulation of natural gas/diesel dual-fuel engine for investigation of performance and emission. J Therm Anal Calorim. 2020. https://doi.org/10.1007/s10973-019-08560-7.
4. Parsa S, Neshat E. Thermodynamic and statistical analysis on the effect of exhaust gas recirculation on waste heat recovery from homogeneous charge compression ignition engines. J Therm Anal Calorim. 2021. https://doi.org/10.1007/s10973-021-10923-y.
5. Dong H, Zhao Z, Fu J, Liu J, Li J, Liang K, et al. Experiment and simulation investigation on energy management of a gasoline vehicle and hybrid turbocharger optimization based on equivalent consumption minimization strategy. Energy Convers Manag. 2020. https://doi.org/10.1016/j.enconman.2020.113518.
6. Ebrahimnataj MR, Tiji AE, Eisapour M, Ali HM, Talebizadehsardari P, Ehteram MA, et al. The effect of soot accumulation and backpressure of an integrated after-treatment system on diesel engine performance. J Therm Anal Calorim. 2022. https://doi.org/10.1007/s10973-021-11135-0.
7. Gao J, Chen H, Tian G, Ma C, Zhu F. An analysis of energy flow in a turbocharged diesel engine of a heavy truck and potentials of improving fuel economy and reducing exhaust emissions. Energy Convers Manag. 2019.https://doi.org/10.1016/j.enconman.2019.01.053
8. Alshammari F, Karvountzis-Kontakiotis A, Pesiridis A, Giannakakis P. Off-design performance prediction of radial turbines operating with ideal and real working fluids. Energy Convers Manag. 2018. https://doi.org/10.1016/j.enconman.2018.06.093.
9. Qi M, Lei X, Wang Z, Ma C. Investigation on the flow characteristics of a VNT turbine under pulsating flow conditions. Proc Inst Mech Eng Part D. 2019;1:1. https://doi.org/10.1177/0954407017744922.
10. Lei X, Qi M, Sun H, Shi X, Hu L. Study on the interaction of clearance flow and shock wave in a turbine nozzle. SAE Technical Paper. 2017. https://doi.org/10.4271/2017-01-1039.
11. Rajoo S. Steady and pulsating performance of a variable geometry mixed flow turbocharger turbine. PhD Thesis. 2007;Imperial College, London.
12. Lee S, Gurgenci H. A comparison of three methodological approaches for meanline design of supercritical CO2 radial inflow turbines. Energy Convers Manag. 2020. https://doi.org/10.1016/j.enconman.2020.112500.
13. Whitfield A, Baines NC. Design of radial turbomachines. Demand Edition;1990.
14. Reunanen A. Experimental and numerical analysis of different volutes in a centrifugal compressor.PhD Thesis. 2001. Acta Universitatis, Lappeenrantaensis.
15. Barnard MCS, Benson RS. Radial gas turbines. Proceedings of IME. 1968; 183: 59–70.
16. Japikse D, Baines NC. Introduction to turbomachinery. Original Edition.Concepts ETI and Oxford;1994.
17. Whitfield A, Noor ABM. Design and performance of vaneless volutes for radial inflow turbines Part 1: non-dimensional conceptual design considerations. J Power Energ. 1994. https://doi.org/10.1243/PIME_PROC_1994_208_035_02.
18. Bhinder FS. Investigation of flow in the nozzle-less spiral casing of a radial inward flow gas turbine. Proc Inst Mech Eng. 1969. https://doi.org/10.1243/PIME_CONF_1969_184_1.
19. Yang M, Martinez-Botas R, Rajoo S, Yokoyama T, Ibaraki S. An investigation of volute cross-sectional shape on turbocharger turbine under pulsating conditions in internal combustion engine. Energy Convers Manag. 2015. https://doi.org/10.1016/j.enconman.2015.06.038.
20. Lee SP, Barrans SM, Jupp ML, Nickson AK. The impact of volute aspect ratio on the performance of a mixed flow turbine. Aerospace. 2017. https://doi.org/10.3390/aerospace4040056.
21. MacGregor SA, Whitfield A, Mohd Noor AB. Design and performance of vaneless volutes for radial inflow turbines. Part 3: Experimental investigation of the internal flow structure. J Power Energ. 1994;1:1. https://doi.org/10.1243/PIME_PROC_1994_208_050_02.
22. Chappie PM, Flynn PF, Mulloy JM. Aerodynamic design of fixed and variable geometry nozzleless turbine casings. J Eng Power. 1980. https://doi.org/10.1115/1.3230212.
23. Whitfield A, Macgregor SA, Noor ABM. Design and performance of vaneless volutes for radial inflow turbines Part 2: Experimental investigation of the mean line performance-assessment of empirical design parameters. J Power Energy. 1994. https://doi.org/10.1243/PIME_PROC_1994_208_.
24. Tabakoff W, Sheoran Y, Kroll K. Flow measurements in a turbine scroll. J Fluids Eng. 1980. https://doi.org/10.1115/1.3240684.
25. Chen H. Design methods of volute casings for turbocharger turbine applications. J Power Energy. 1996. https://doi.org/10.1243/PIME_PROC_1996_210_022_02.
26. Abidat M, Hamidou MK, Hachemi M, Hamel M. Design and flow analysis of radial and mixed flow turbine volutes. In proceedings of ASME turbo expo:power for land, sea and air conference,Germany: 2008. Paper no.GT2008–50503.
27. Gu F, Engeda A, Benisek E. A comparative study of incompressible and compressible design approaches of radial infow turbine volutes. Proc Inst Mech Eng Part A: J Power Energy. 2001; https://doi.org/10.1243/0957650011538730.
28. Suhrmann JF, Peitsch D, Gugau M, Heuer T. On the effect of volute tongue design on radial turbine performance. In proceedings of ASME turbo expo. Denmark: 2012. Paper no GT2012–69525.
29. Martinez-Botas RF, Pullen KR, Shi F. Numerical calculations of a turbine volute using A 3-D Navier–Stokes solver. In Proceeding of ASME: International Gas Turbine and Aeroengine congress and exhibition,UK:1996. Paper no. 96-GT-66.
30. Simpson AT, Spence SWT, Watterson JK. A comparison of the flow structures and losses within vaned and vaneless stators for radial turbines. J Turbomach. 2009; https://doi.org/10.1115/1.2988493.
31. Lee SP, Jupp ML, A. K. Nickson. The influence of secondary flow structures in a turbocharger turbine housing in steady state and pulsating flow conditions.In proceeding of international Conference on Mechanical and Aerospace Engineering, ICMAE. 2016; https://doi.org/10.1109/icmae.2016.7549526.
32. Meghnine MA, Hamidou MK, Hamel M. Influence of the volute cross-sectional shape on mixed inflow turbine performances. J Adv Mech Eng. 2017. https://doi.org/10.1177/1687814017708174.
33. Lee SP, Barrans SM, Nickson AK. The impact of volute aspect ratio and tilt on the performance of a mixed flow turbine. Proc Inst Mech Eng Part A: J Power Energy. 2021; https://doi.org/10.1177/0957650921998228
34. Padzillah MH. Experimental and numerical investigation of an automotive mixed flow turbocharger turbine under pulsating flow conditions. PhD Thesis. 2014. Imperial College, London.
35. Glassmann AJ. Basic turbine concepts in turbine design and application. Vol.1, NASA SP- 290; 1972.

36. Szymko S. The development of an eddy current dynamometer for evaluation of steady and pulsating turbocharger turbine performance. PhD Thesis. 2006. Imperial College, London.
37. Dean.W.R. The motion of fluid in a curved pipe. Lond Edinb Dublin Philos Mag J Sci. 1927; https://doi.org/10.1080/14786440708564324.
38. Chandratilleke TT, Nadim N, Narayanaswamy R. Analysis of secondary flow characteristics and hydrodynamic instability in fluid flow through curved ducts. In: Proceeding of international conference on heat transfer, fluid mechanics and thermodynamics, Mauritius. 2011;pp 704–710.